Model-Based Reconstruction of Magnetic Resonance Spectroscopic Imaging

by

Itthi Chatnuntawech

B.S. Electrical and Computer Engineering, Carnegie Mellon University (2011)

B.S. Biomedical Engineering, Carnegie Mellon University (2011)

Submitted to the Department of Electrical Engineering and Computer Science

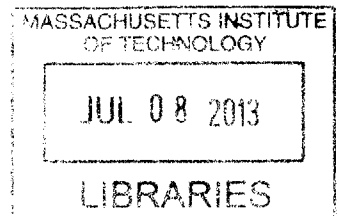in partial fulfillment of the requirements for the degree of

Master of Science in Electrical Engineering and Computer Science

at the

MASSACHUSETTS INSTITUTE OF TECHNOLOGY

June 2013

The author hereby grants to MIT permission to reproduce and distribute publicly

paper and electronic copies of this thesis document in whole or in part.

Author..

Department of Electrical Engineering and Computer Science

April 29, 2013

Certified by...

Elfar Adalsteinsson

Associate Professor of Electrical Engineering and Computer Science

Associate Professor of Institute of Medical Engineering and Science

Thesis Supervisor

Accepted by...

Leslie A. Kolodziejski

Chair, Department Committee on Graduate Students

Model-Based Reconstruction of Magnetic Resonance Spectroscopic Imaging

by

Itthi Chatnuntawech

Submitted to the Department of Electrical Engineering and Computer Science

on April 29, 2013, in partial fulfillment of the

requirements for the degree of

Master of Science in Electrical Engineering and Computer Science

Abstract

Magnetic resonance imaging (MRI) is a medical imaging technique that is used to obtain images of soft tissue throughout the body. Since its development in the 1970s, MRI has gained tremendous importance in clinical practice because it can produce high quality images of diagnostic value in an ever expanding range of applications from neuroimaging to body imaging to cancer.

By far the dominant signal source in MRI is hydrogen nuclei in water. The presence of water at high concentration (~50M) in body tissue, combined with signal contrast modulation induced by the local environment of water molecules, accounts for the success of MRI as a medical imaging modality. As opposed to conventional MRI, which derives its signal from the water component, magnetic resonance spectroscopy (MRS) acquires the magnetic resonance signal from other chemical components, most frequently various metabolites in the brain, but also signals from tumors in breast and prostate. The spectroscopic signal arises from low concentration (~1-10mM) compounds, but in spite of the challenges posed by the resulting low signal-to-noise ratio (SNR), the development of MRS is motivated by the desire to directly observe signal sources other than water. The combination of MRS with spatial encoding is called magnetic resonance spectroscopic imaging (MRSI). MRSI captures not only the relative intensities of metabolite signals at each voxel, but also their spatial distributions.

While MRSI has been proven to be clinically useful, it suffers from fundamental tradeoffs due to the inherently low SNR, such as long acquisition time and low spatial resolution. In this thesis, techniques that combine benefits from both model-based reconstruction methods and regularized reconstructions with prior knowledge are proposed and demonstrated for MRSI. These methods address constraints on acquisition time in MRSI by undersampling data during acquisition in combination with improved image reconstruction methods.

Thesis Supervisor: Elfar Adalsteinsson

Title: Associate Professor of Electrical Engineering and Computer Science

Associate Professor of Institute of Medical Engineering and Science

Acknowledgements

I am very grateful for all the people who have been a big part of my graduate student life at MIT. First, I wish to express my most sincere gratitude to Prof. Elfar Adalsteinsson for his mentorship and guidance, which have tremendously impacted on my professional development.

I have had the wonderful opportunity to work with a great group of people in the Magnetic Resonance Imaging Group: Obaidah Abuhashem, Berkin Bilgic, Divya S. Bolar, Audrey Peiwen Fan, Shao Ying Huang, Trina Kok, Paula Montesinos, Christin Y. Sander, and Filiz Yetisir. Thank you all for providing an enjoyable and pleasurable environment over the past year.

I am greatly indebted to Berkin for his thoughtful ideas, invaluable suggestions, and perceptive insights that have helped me advanced my research skills. Many of our discussions contributed significantly not only to my research in general, but in particular, to this thesis.

I would also like to thank Paula, Audrey, Shao Ying, Christin, and Trina for plenty of assistance with various aspects of my life. Thank you all for bringing happiness to the office. My social life would have suffered without them.

I also want to thank Prof. Kawin Setsompop, Stephen F. Cauley, and Borjan A. Gagoski for collaborations on various projects. Thank you Kawin for introducing me to the MRI group. Thank you Steve for teaching me various useful mathematical techniques and insights. And thank you Borjan for helping me with the MRSI project.

Thanks to my friends and colleagues who have made my graduate student life at MIT so enjoyable. In particular, I am very thankful to Tarek Aziz Lahlou for numerous stimulating, thoughtful, and endless discussions we have had. These discussions on both classes and our research projects greatly influenced my research thought process.

I also wish to thank my friends in Thailand for their true friendship. Thank you all for always being there for me and keeping me sane.

Finally, I am eternally thankful for my parents and my sister for their unwavering love, emotional support, and constant encouragement.

Contents

List of Figures

Chapter 1

Magnetic Resonance Spectroscopic Imaging

By far the dominant signal source in MRI is hydrogen nuclei in water. The presence of water at high concentration (~50M) in body tissue, combined with signal contrast modulation induced by the local environment of water molecules, accounts for the success of MRI as a medical imaging modality. As opposed to conventional MRI, which derives its signal from the water component, magnetic resonance spectroscopy (MRS) acquires the magnetic resonance signal from other chemical components, most frequently various metabolites in the brain, but also signals from tumors in breast and prostate. The spectroscopic signal arises from low concentration (~1-10mM) compounds, but in spite of the challenges posed by the resulting low signal-to-noise ratio (SNR), the development of MRS is motivated by the desire to directly observe signal sources other than water.

In most MRS brain applications, the primary metabolites include N-acetyl aspartate (NAA) - a marker of neuronal density, creatine (Cr) - an energy supplier to all cells in the body, choline (Cho) - a water-soluble necessary nutrient for basic functions of memory and muscular system, and lactate - an end product of anaerobic metabolism [1, 2]. The magnetic resonance signal acquired from a particular chemical component can be distinguished from that obtained from other components because of consequences of the chemical shift phenomenon, which is explained in detail in the following subsection. With MRS, the information about cellular activities could be inferred in addition to the structural information obtained from the conventional MRI.

13

The combination of MRS with spatial encoding is called magnetic resonance spectroscopic imaging (MRSI). MRSI captures not only the relative intensities of metabolite signals at each voxel, but also their spatial distributions (metabolite maps). Irregular changes of the metabolite concentration in specific brain regions can be used to indicate specific physiological abnormalities. For instance, a dramatic reduction in NAA concentration in the specific brain regions is a precursor of many neurodegenerative diseases such as X-linked adrenoleukodystrophy (X-ALD) [3], multiple sclerosis (MS) [4, 5], and Alzheimer's disease [6, 7]. A creatine deficiency is an indicator of brain tumors such as gliomas, astrocytomas, and meningiomas [8]. An elevation of choline is related to acute demyelination diseases and a certain type of brain tumor [9, 10]. An increased lactate level indicates an abnormal metabolism [2, 11].

This chapter introduces basic concepts of magnetic resonance spectroscopic imaging (MRSI), which consist of a chemical shift, J-coupling, a magnetic field inhomogeneity, water and lipid resonances, noise in MRI, and a signal-to-noise ratio (SNR). Then, a conventional MRSI acquisition is briefly described. Finally, a brief description of the problem statement and the organization of this thesis with bibliographical contributions are presented at the end of this chapter.

1.1 Introduction to Magnetic Resonance Spectroscopic Imaging (MRSI)

1.1.1 Chemical Shift

In nuclear magnetic resonance (NMR) spectroscopy, the chemical shift is defined as a small displacement of the resonant frequency of a nucleus caused by an electron shielding. Although a heterogeneous object is placed in the homogenous main magnetic field (B_0), all nuclei do not experience the same field strength because of the shielding effect created by the orbital motion of the surrounding electrons in response to the applied B_0 field [2, 12]. In fact, shielding electrons act to shield the valence electrons from the force of attraction exerted by *any* applied magnetic field, thus different nuclei in that object experience different amounts of shielding. The effective field (B_{eff}) experienced by a particular nucleus can be expressed as

14

$$B_{eff} = B_0(1 - \sigma) \qquad (1\text{-}1)$$

where σ represents the shielding constant, which is dependent on the chemical environment. It follows from the Larmor relationship that

$$
\begin{aligned}
\omega_{eff} &= \gamma B_{eff} \\
&= \gamma B_0(1 - \sigma) \\
&= \omega_0(1 - \sigma) \\
&= \omega_0 - \sigma\omega_0 \qquad (1\text{-}2)
\end{aligned}
$$

where γ is the gyromagnetic ratio, and $\sigma\omega_0$ is the displacement of the resonant frequency, which is directly proportional to the B_0 field. The chemical shift δ is usually expressed in parts per million (ppm) to accentuate the comparison of results. Let ω_{ref} and ω_s be the reference frequency and the resonant frequency of a specific sample, respectively. The chemical shift can be computed as

$$
\begin{aligned}
\delta &= \frac{\omega_s - \omega_{ref}}{\omega_{ref}} \times 10^6 \\
&= \frac{\omega_0(1 - \sigma_s) - \omega_0(1 - \sigma_{ref})}{\omega_0(1 - \sigma_{ref})} \times 10^6 \\
&= \frac{\sigma_{ref} - \sigma_s}{1 - \sigma_{ref}} \times 10^6 \\
&\approx (\sigma_{ref} - \sigma_s) \times 10^6 \qquad (1\text{-}3)
\end{aligned}
$$

where the approximation is acceptable because $\sigma_{ref} \ll 1$.

Both Equation (1-2) and (1-3) explain why the NMR spectrum obtained from the MRI scanner shows peaks at different frequencies instead of a single peak at exactly one frequency. Figure 1-1 shows the effect of the chemical shift phenomenon on the synthetic ^{1}H NMR spectrum of the acetic acid (CH_3COOH). The chemical shift axis in the NMR spectroscopy is shown in the ppm unit, and the frequency axis is flipped due to historical reasons. Specifically, the frequency decreases from left to right. There are two peaks at two different frequencies because the single proton in the carboxyl group ($-COOH$) experiences a different chemical shift than the protons in the methyl group ($-CH_3$). Specifically, the valency of the oxygen atoms in the carboxyl group leads to less

shielding for the single proton in this group compared to the protons in the carbonyl group. With less shielding, the resonant frequency deviates more from the reference frequency at 0 ppm than that of the protons in the carbonyl group. It can also be seen that the area under the carboxyl peak is approximately three times lower than the area under the methyl peak because the area under each peak positively correlates with the number of nuclei resonating at this specific frequency.

1.1.2 J-Coupling

Not only the chemical shifts due to electron shielding effects, but also an indirect dipole-dipole coupling or J-coupling have a major impact on the appearance of the NMR spectrum. Interactions between nuclei, which are physically close to one another, lead to peak-splitting or line-splitting in the NMR spectrum [2, 13]. Figure 1-2 shows the effect of J-coupling on the synthetic ^{1}H NMR spectrum of lactate. The single proton in the −CH group couples with each of the three methyl protons resulting in the peak-splitting into four peaks. Similarly, the signal corresponding to the methyl protons is split into two peaks due to an interaction between the methyl protons and the single proton in the −CH group.

1.1.3 Magnetic Field Inhomogeneity

The magnetic field inhomogeneity affects the NMR spectrum by not only shifting all peaks along the frequency axis by approximately the same amount, but also modifying a spectral linewidth of each peak, a width at half maximum. Specifically, the magnetic field inhomogeneity leads to dephasing of the time signal called free induction decay (FID). The dephasing of the FID results in an increase in the spectral linewidth. In practice, the maximum acceptable spectral linewidth for quantifiable MRSI data is equal to 0.1 ppm [14]. Consequently, the magnetic resonance signal from particular anatomical regions with strong magnetic field inhomogeneity such as tissue-bone and tissue-air boundaries is not collected in some quantification MRSI experiments.

16

1.1.4 Water and Lipid Resonances

In ^{1}H-MRSI, water and lipid produce a much larger signal than that from target metabolites. With the magnetic field inhomogeneity, the artifacts arose from water components could contaminate metabolite signals. To mitigate such artifacts, water suppression techniques such as frequency selective RF pulses are adopted [14]. In addition to water artifacts, artifacts from the lipid signal due to a point spread function (PSF) further contaminate metabolite signals. In practice, it is not possible to achieve an infinite sampling extent of k-space, where k represents a spatial-frequency variable, because spatial resolution is constrained by the total acquisition time and low signal-to-noise ratio (SNR) of the metabolite signals [15]. Such the finite sampling extent can create Gibb's ringing artifacts from truncation in the spatial-frequency domain. In ^{1}H-MRSI, lipid components in subcutaneous tissues, which produce a signal that are as much as 1000 times stronger than metabolite signals, bleed into nearby voxels contaminating the desired metabolite signals. To achieve higher quality of MRSI data, various lipid suppression techniques, which aim to attenuate truncation artifacts arose from lipid components, have been proposed such as the inversion recovery [16, 17], the outer-volume suppression (OVS) [18, 19], the selective brain-only excitation [20, 21], and the combination between the dual-density sampling and the lipid-basis orthogonality [15].

1.1.5 Noise Sources and Signal-to-Noise Ratio

There are various main sources of noise in MRI that affect imaging quality. They consist of the body noise, the noise of the receiver electronics, and thermal noise of the coil. The dominating source of noise is due to thermal fluctuations of electrolytes in the body (i.e., the body noise). The noise is typically characterized as being additive, Gaussian distributed, and white [12]. The resulting image quality is measured by the signal-to-noise ratio (SNR). While SNR is typically defined as the ratio between the signal power and the noise power in statistical communication community, it is defined differently in the MR community as

$$SNR \triangleq \frac{signal\ amplitude}{\sigma_{noise}} \qquad (1\text{-}4)$$

17

where σ_{noise} is the standard deviation of the noise. Because the magnetic resonance signal from metabolites has much lower signal strength than that from the water component, noise greatly affects the resulting image quality in MRSI. Consequently, it is desirable to achieve high SNR in order to avoid the metabolites from being buried in noise, which leads to an improvement in the MRSI reconstruction. One way to increase SNR is to increase the acquisition time (e.g., to acquire multiple averages) and use a larger voxel size.

1.1.6 Example of MRSI data

As opposed to the conventional MRI that focuses on contributions from the water component, magnetic resonance spectroscopy aims to acquire the magnetic resonance signal from metabolites. For single voxel MRS (SV-MRS), the magnetic resonance signal at a specific spatial location is acquired over a certain period of time and yields a spectrum with multiple peaks at different frequencies due to the effects of the chemical shift phenomenon, J-coupling, and other complications. Figure 1-3 shows a noise-free, lipid-free, water-suppressed synthetic spectrum with signal components from compounds observed in human brain tissues.

As an extension of SV-MRS, magnetic resonance spectroscopic imaging (also known as multi-voxel spectroscopy) has been developed and widely used in many clinical applications especially in the study of in vivo metabolism. MRSI captures not only the relative intensities of metabolite signals at each voxel, but also their spatial distributions. Figure 1-4 shows NAA, Cr, and Cho maps that were extracted from the MRSI data acquired fully-sampled at 1.5 Tesla with a total scan time of 15:20 minutes and a resolution of 1.1 cc. The water resonance was suppressed using spin-echo spectral-spatial pulses. Inversion recovery with an inversion time of 170 milliseconds was used to suppress lipid components. The magnitude of each pixel in these metabolite maps is computed by summing the absolute value of the spectrum over the frequency range of the metabolite of interest. Figure 1-5 shows a spectroscopic image obtained by summing the absolute value of the spectra over the whole frequency range, and the corresponding spectra from the voxels within the black box. These maps and spectra were extracted from the same data set as those in Figure 1-4.
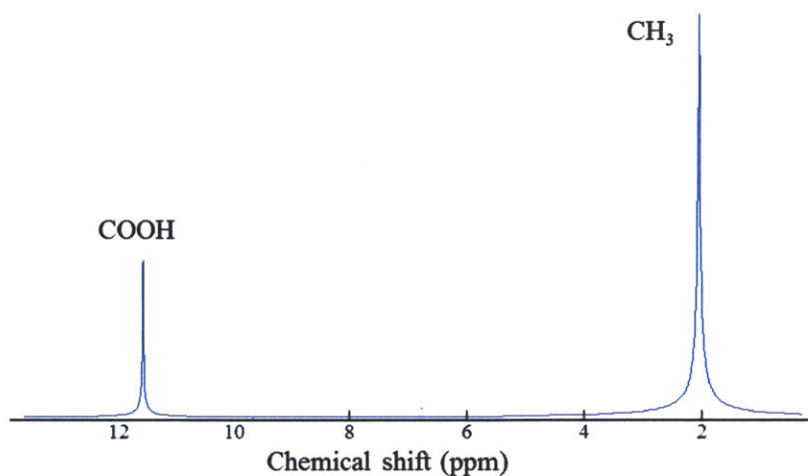
Figure 1-1: The effect of the chemical shift phenomenon without J-coupling on the synthetic ^{1}H NMR spectrum of acetic acid (CH_3COOH). The single proton in the carboxyl group ($-COOH$) experiences a different chemical shift than the protons in the methyl group ($-CH_3$) due to the different chemical environment [12].
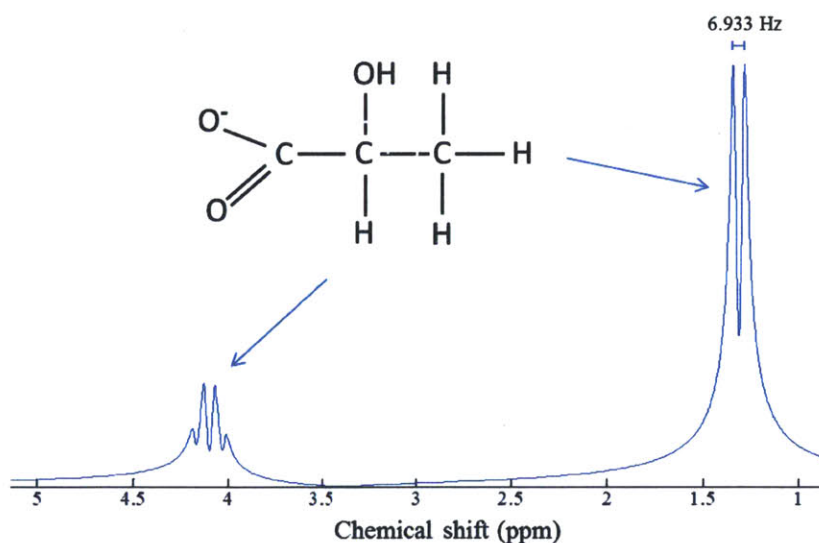
Figure 1-2: The effect of J-coupling on a synthetic ^{1}H NMR magnitude spectrum of lactate that was acquired at three Tesla. The durations of the acquisition window were equal to 0.25 seconds (red) and 7.77 seconds (blue) with the bandwidth of 3.003 kHz. The single proton in the $-CH$ group couples with each of the three methyl protons resulting in the peak-splitting into four peaks. Similarly, the signal corresponding to the methyl protons is split into two peaks due to interaction between the methyl protons and the single proton in the $-CH$ group.

19
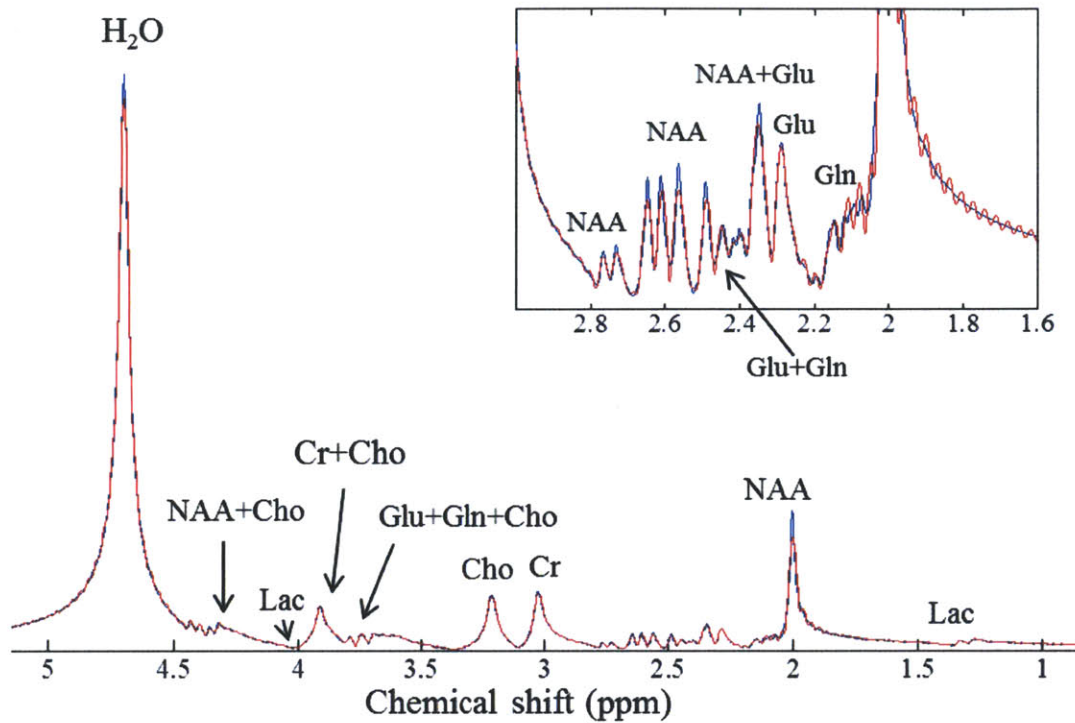
Figure 1-3: A noise-free, lipid-free, water-suppressed synthetic spectrum with signal components from compounds observed in human brain tissues. This data set was acquired at three Tesla. The durations of the acquisition window were equal to 0.25 seconds (red) and 7.77 seconds (blue) with the bandwidth of 3.003 kHz.
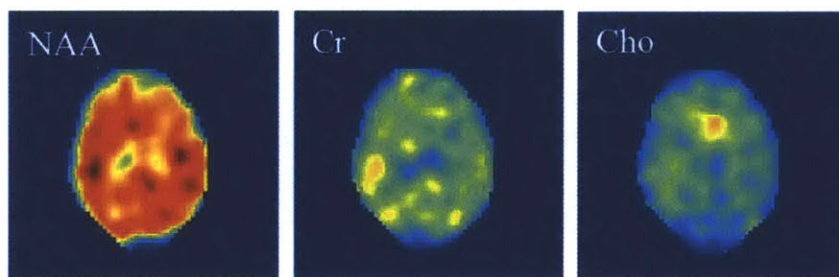
Figure 1-4: NAA map (left), Cr map (middle), and Cho map (right) that were extracted from the in vivo MRSI data acquired fully-sampled at 1.5 Tesla.
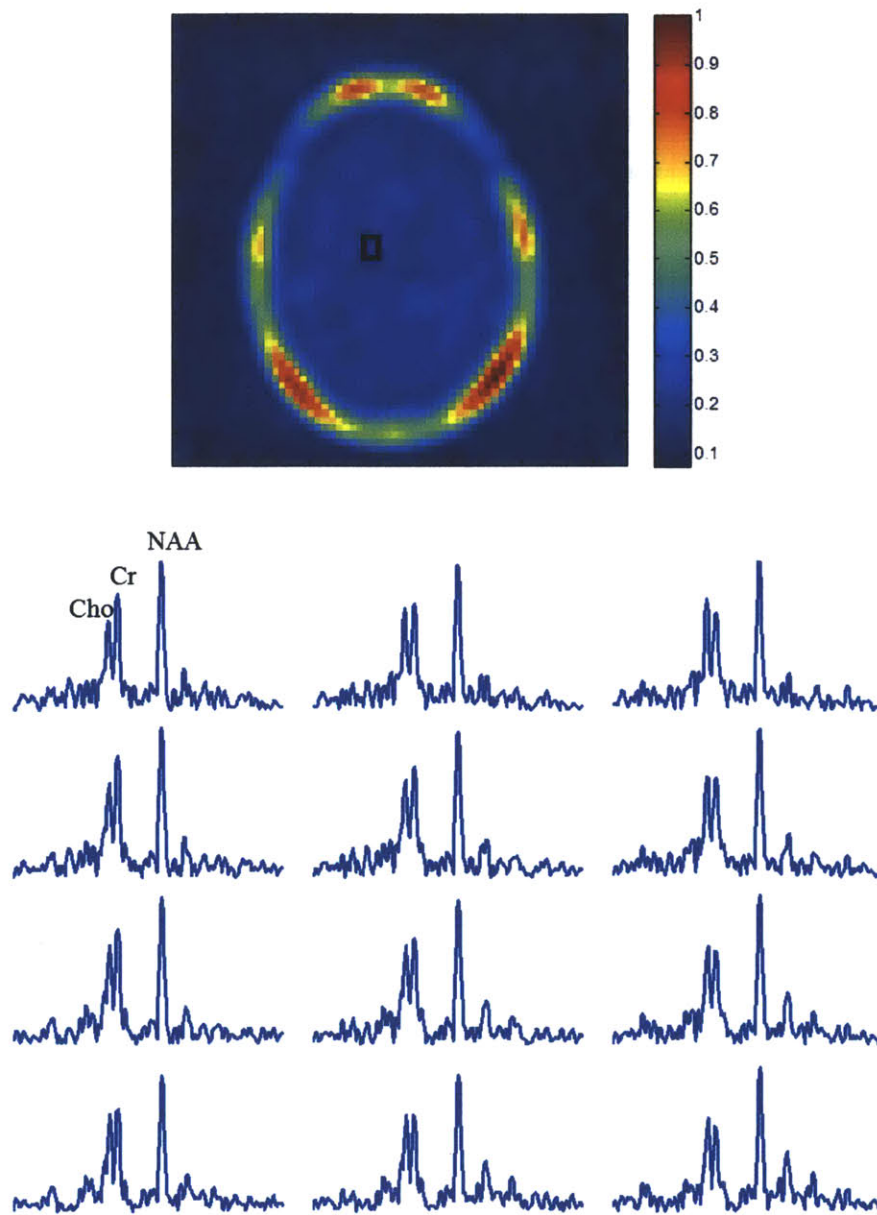
Figure 1-5: Spectroscopic image obtained by summing the absolute value of the spectra over the whole frequency range (top), and the corresponding spectra from the voxels within the black box (bottom) of the in vivo MRSI data acquired fully-sampled at 1.5 Tesla.

1.2 Conventional Magnetic Resonance Spectroscopic Imaging Acquisition

While magnetic resonance spectroscopic imaging has been proven to be clinically useful [5, 10, 22-25], it suffers from fundamental tradeoffs due to the inherently low SNR, such as the long acquisition time and low spatial resolution. Since MRSI acquires a time dimension(s) in addition to the three dimensions normally acquired in the conventional MRI, the acquisition time is greatly increased. Moreover, multiple averages are normally acquired in order to increase the SNR to an acceptable range, which further increases the acquisition time.

The conventional procedure to acquire the MRSI data is to move to a specific (k_x, k_y, k_z) location and collect the magnetic resonance signal at that location over a certain period of time. Then, the same procedure is repeated at different locations until the resolution and field-of-view (FOV) requirements are satisfied. This method allows acquisition only at a specific (k_x, k_y, k_z) location for each repetition time (TR). By staying at only one (k_x, k_y, k_z) location for each excitation, an analog to digital converter (ADC) oversamples the data. Thus, the acquisition process can be sped up by getting time samples at more than one spatial location during a single TR period, while satisfying the Nyquist constraint. The spiral-based k-space traversal is one of the most efficient ways to perform such a task [1, 26].

1.3 Problem Statement and Outline with Bibliographical Notes

1.3.1 Problem Statement

Even with the spiral trajectory, the acquisition time is still considerably long in practice. In this work, two model-based reconstruction methods are proposed to not only further reduce the acquisition time, but also provide an improvement in the reconstruction quality compared to that of existing methods. With parametric modeling, only a few parameters are needed to describe the underlying data. Thus, an undersampling of the k-space data becomes possible. By undersampling the k-space data, both aliasing and undersampling artifacts are introduced to the data in the object domain, which corrupts the observed data. With the presence of such artifacts, the conventional reconstruction methods, such as methods that seek for a minimum-norm solution, lead to an inaccurate reconstruction. In order to improve the reconstruction accuracy, the proposed methods incorporate prior information into the reconstruction process. With fewer parameters to estimate, the reconstruction process becomes more robust.

1.3.2 Thesis Outline

The detailed structure of this thesis is as follows. Chapter 2 is a review of a regularized optimization. It presents a canonical least-squares problem and an unconstrained penalty function approximation problem. In addition, effects of various penalty functions on the solution of the penalty function approximation problem are illustrated. Toward the end of the chapter, a few examples of the unconstrained penalty function approximation problem formulation for various applications including magnetic resonance spectroscopic imaging are presented.

Chapter 3 reviews a mathematical model for a typical magnetic resonance spectroscopic imaging spectrum. It then describes the proposed reconstruction procedure under this mathematical model in detail. We demonstrated on the experimental data obtained from a healthy human subject that the proposed method yields the more accurate reconstruction compared to that of the conventional least-squares method.

Chapter 4 reviews a conventional mathematical model and presents an alternative mathematical model of metabolite maps. The relationship between these two models is then explained. Next, the reconstruction procedure is described in detail. Finally, the performance of the proposed method is compared to that of the conventional method on two data sets, which consist of a numerical magnetic resonance spectroscopic imaging phantom and in vivo acquisitions, using the root-mean-square error as a criterion.

1.3.3 Bibliographical Notes

The contents of Chapter 3 appear in:

- I. Chatnuntawech, B. Bilgic, E. Adalsteinsson. Undersampled Spectroscopic Imaging with Model-based Reconstruction. International Society for Magnetic Resonance in Medicine 21st Scientific Meeting, Salt Lake City, Utah, USA, 2013.

The contents of Chapter 4 appear in:

- I. Chatnuntawech, B. Bilgic, B.A. Gagoski, T. Kok, A.P. Fan, E. Adalsteinsson. Metabolite Map Estimation from Undersampled Spectroscopic Imaging Data using N-Compartment Model. International Society for Magnetic Resonance in Medicine 21st Scientific Meeting, Salt Lake City, Utah, USA, 2013.

Chapter 2

Regularized Reconstruction

Under certain conditions, a signal can completely be characterized and recoverable from its samples equally spaced in the same domain. Specifically, if a bandlimited signal is uniformly sampled above the Nyquist rate, the perfect reconstruction of such a signal is guaranteed [27]. However, if a signal is sampled at or below the Nyquist rate and/or nonuniformly sampled, it becomes much harder to achieve a highly accurate reconstruction without any prior information. One way to improve the reconstruction accuracy is to incorporate prior knowledge of the data into the reconstruction process.

In magnetic resonance imaging, the data is typically acquired below the Nyquist rate because of limitations on both physical and physiological constraints. Consequently, aliasing and undersampling artifacts distort the underlying data and greatly reduce the reconstruction quality. In order to mitigate such contaminations, reconstruction methods that exploit prior knowledge of the data have been proposed. Popular prior knowledge exploited by the compressed sensing community is sparsity [25].

In this chapter, mathematical definitions of norm, sparsity, and compressibility are presented. Using these definitions, a canonical least-squares problem and an unconstrained penalty function approximation problem are described. The effects of various penalty functions on the solution of the penalty function approximation problem are also illustrated. This chapter concludes with a few examples of the unconstrained penalty function approximation problem setup for various applications including magnetic resonance spectroscopic imaging.

2.1 Norm, Sparsity, and Compressibility

Definition 2.1.1. *A norm, denoted by a symbol* $\|.\|$, *is defined as a function that maps an element in a vector space V over a field F to a nonnegative real number with the following properties* [28, 29]:

For all $a \in F$ and all $x, y \in V$,

1. $\|ax\| = |a|\|x\|$

2. $\|x + y\| \leq \|x\| + \|y\|$

3. *If $\|x\| = 0$, then x is the zero vector.*

4. $\|x\| \geq 0$

The most widely used norms in the MR community are the p-norm, the Manhattan norm, and the Euclidean norm. The p-norm is defined as

$$\|x\|_p = \left(\sum_i |x_i|^p\right)^{\frac{1}{p}} \tag{2-1}$$

where x_i is the ith element of x. The Manhattan norm (also called the l_1 norm) of a vector x is defined as

$$\|x\|_1 = \sum_i |x_i| \tag{2-2}$$

where x_i is the ith element of x. The Euclidean norm (also called the l_2 norm) of a vector x is defined as

$$\|x\|_2 = \sqrt{\sum_i |x_i|^2} \tag{2-3}$$

where x_i is the ith element of x. The l_1 norm and the l_2 norm are special cases of the p-norm when p is equal to one and two, respectively. Each type of a norm has its own characteristics, which can be seen using the notion of a unit ball. The unit ball is defined as the set of all vectors of unit norm. For instance, the unit ball in $\mathfrak{R}^2$ becomes a diamond for the l_1 norm, whereas it becomes a unit circle for the l_2 norm, as shown in Figure 2-1.

26

The effects of having such different characteristics will be prominent when various types of norm are used in the reconstruction process. For instance, when the l_1 norm is imposed on the data x, the reconstructed data $\hat{x}$ that is obtained by solving the regularized optimization problem in the standard form tends to be sparse.

Definition 2.1.2. *A vector* x *is K-sparse if it can be represented in a basis by at most K nonzero coefficient. Alternatively, a vector* x *is K-sparse if its support is of cardinality less than or equal to K* [30].

The sparsity of a signal can be measured by the cardinality, denoted $card(.)$, which counts the number of nonzero values of a signal. By using the cardinality notation, a K-sparse signal x must satisfy the following property

$$card(x) = \sum_i 1(x_i \neq 0) \leq K \tag{2-4}$$

where $1(.)$ is an indicator function, and x_i is the ith element of x. Examples of a sparse signal are an impulse and a summation of a few impulses. A more complicated example of a sparse signal, which is widely recognized in the MR community, is a piecewise constant signal in a finite-differences domain.

Most commonly encountered signals are not sparse in any transform basis, so the notion of the real sparsity is hard to find in practice. Consequently, the notion of compressibility, which can be interpreted as a relaxation of sparsity, is introduced. A signal is *compressible* if it can be represented using only a few dominating coefficients. Figure 2-2 shows a sparse signal (top) and a compressible signal (bottom). The notion of sparsity and compressibility is very important because it can be used as a prior knowledge to help improve the reconstruction accuracy.
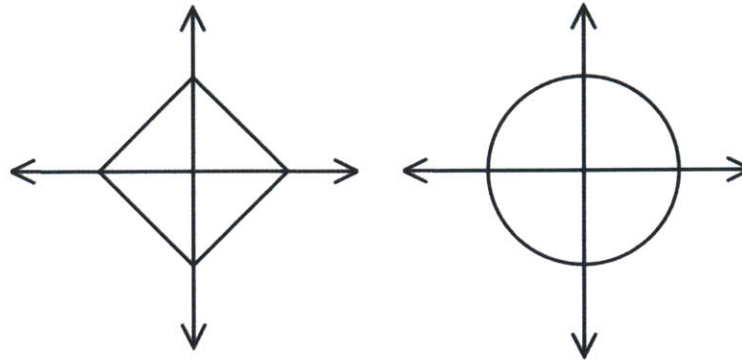
Figure 2-1: Unit balls in the l_1 norm (left) and l_2 norm (right). The set of all vectors of unit norm is a diamond and a unit circle for the l_1 and l_2 norm, respectively.
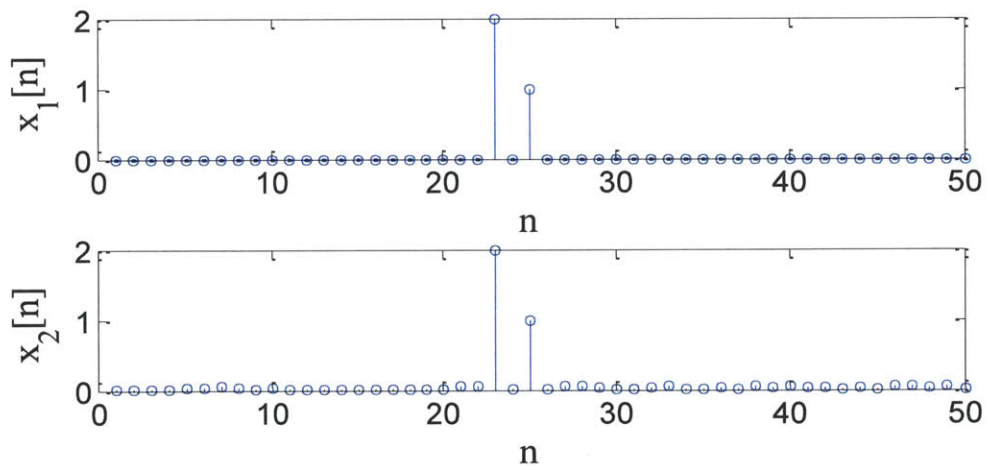
Figure 2-2: A sparse signal $x_1[n]$ has only two nonzero components (top). A compressible signal $x_2[n]$ has two dominating coefficients and a bunch of small coefficients (bottom).

2.2 Least-Squares Problem

The canonical least-squares problem involves solving the system of linear equations $Ax = b$, where A is an $m \times n$ matrix; x is an $n \times 1$ vector; and b is an $m \times 1$ vector, in the least-squares sense. If b lies in a column space of A (i.e., $b \in R(A)$) where $R(A)$ is the range space of A, there either be a unique solution or infinitely many solutions to this linear system. If $b \notin R(A)$, the solution to such a system does not exist. In this case, it may be desirable to find an approximate solution by solving the following least-squares optimization problem

$$\hat{x} = \underset{x}{\mathrm{argmin}} \quad \|Ax - b\|_2^2 \tag{2-5}$$

A solution to this optimization problem can be interpreted as an exact solution to the modified system of linear equations $Ax = \tilde{b}$ where $\tilde{b}$ is a projection of b onto $R(A)$.

When the linear system is underdetermined (i.e., A is a *fat* matrix $(m < n)$), and the null space of a matrix A, denoted $N(A)$, is not empty, there exist infinitely many solutions to the least-squares optimization problem in Equation (2-5). In this case, we may prefer one solution to other solutions depending on a specific application. Regularization is one technique that is widely adopted to select the solution with the specific property among all other solutions.

2.3 Regularized Reconstruction

Regularization is a common scalarization technique that introduces additional information so that the condition of the problem is improved. Many regularization techniques involve incorporating prior knowledge of the data into the reconstruction to improve the reconstruction accuracy. By applying the duality theory and regularizations, the following *unconstrained penalty function approximation problem* is solved instead of the problem shown in Equation (2-5)

$$\hat{x} = \underset{x}{\text{argmin}} \quad \|Ax - b\|_2^2 + \lambda_k \sum_k \phi_k(x) \qquad (2\text{-}6)$$

where A is an $m \times n$ matrix; x is an $n \times 1$ vector; b is an $m \times 1$ vector; ϕ_k is the kth penalty function; and λ_k is a nonnegative dual variable (also called a regularization parameter) corresponding to the kth penalty function. The prior knowledge of the data is taken into account through the penalty functions that appear in the objective function, as shown in Equation (2-6).

2.3.1 Effects of Various Penalty Functions on the Solution of the Penalty Function Approximation Problem

For simplicity of this discussion, let us consider the constrained penalty function approximation problem of the form

$$\underset{x}{\text{minimize}} \quad \phi(x) \qquad (2\text{-}7)$$

$$\text{subject to } Ax = b$$

where A is an $m \times n$ matrix; x is an $n \times 1$ vector; b is an $m \times 1$ vector; and ϕ is a penalty function that maps an element in a vector space to a real number. For the sake of discussing the effects of different penalty functions on the solution, we assume that there are infinitely many solutions to the system of linear equations $Ax = b$.

The penalty function $\phi(x)$ assesses a cost for each component of x. In the penalty function approximation problem, the total penalty incurred by x is minimized. Consequently, the characteristics of the chosen penalty function have a high impact on the solution of the penalty function approximation problem. If ϕ is small for a certain

30

range of values, it means we do not care much if elements of x have nonzero values in this range. In contrast, if ϕ is large for a certain range of values, it means we try to avoid elements of x from having nonzero values in such a range [29].

As an example in a one-dimensional case, let us consider two commonly used penalty functions in the MR community: $\phi_1(x) = \|x\|_1$ and $\phi(x) = \|x\|_2^2$, where $x \in \Re$. On the one hand, ϕ_1 assesses a relatively high cost compared to ϕ_2 for a small value of x. On the other hand, ϕ_1 assesses a much lower cost than that of ϕ_2 for a high value of x, as shown in Figure 2-3. It is this difference in penalty for a small and large value of x that shapes the solution of the penalty function approximation problem. By using the l_1 norm as a penalty function, the solution will have a lot more zero elements compared to that of the l_2 norm. In other words, the solution of the l_1 regularized problem will be relatively sparse. In contrast, the solution of the l_2 regularized problem will have relatively fewer large elements due to its relatively high penalty on large values.
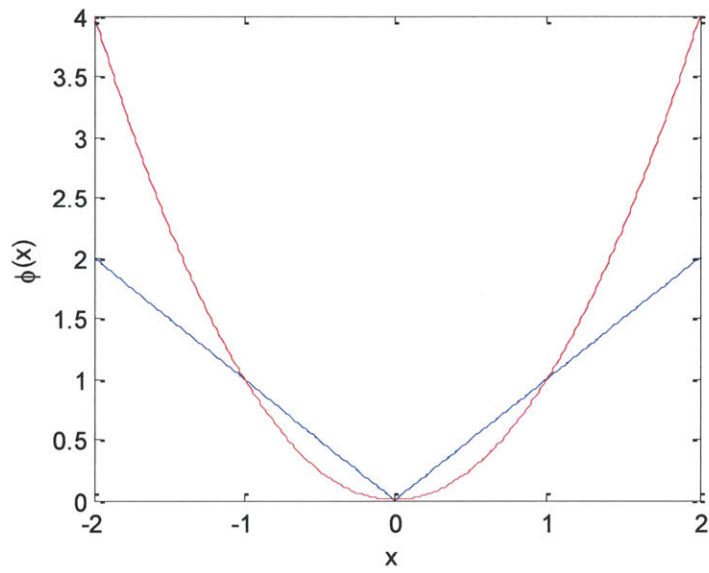
Figure 2-3: The l_1 norm penalty function (blue) and the l_2 norm penalty function (red). The l_1 norm penalty function put a relatively high weight compared to the l_2 norm penalty function for a small value of x, whereas it put a relatively low weight for a large value of x.

2.3.2 Choices of Penalty Function for Various Applications

The penalty functions are chosen differently depending on specific applications. For example, in many communication applications, it is desirable to construct the minimum Euclidean norm solution among all other solutions. In this case, the quadratic penalty function is used. The optimization problem then becomes

$$\hat{x} = \underset{x}{\text{argmin}} \quad \|Ax - b\|_2^2 + \lambda\|x\|_2^2. \tag{2-8}$$

The Moore-Penrose pseudoinverse is one of many common techniques used to construct the solution with minimum energy. On the contrary, in the compressed sensing community, it is often the case that a signal of interest is sparse or compressible. As a result, it is tempted to use a cardinality function as a penalty function. This choice of penalty function leads to the following optimization problem

$$\hat{x} = \underset{x}{\text{argmin}} \quad \|Ax - b\|_2^2 + \lambda\, card(x). \tag{2-9}$$

Unfortunately, the cardinality function is not a convex function of its input and not differentiable at the origin due to a jump-discontinuity. In practice, the l_1 norm, which is a relaxation of the cardinality function, is used as the penalty function instead in order to turn the problem into the convex optimization problem [30, 31]. With this modification, a sparse or compressible signal is usually reconstructed from a subset of samples by solving

$$\hat{x} = \underset{x}{\text{argmin}} \quad \|Ax - b\|_2^2 + \lambda\|x\|_1. \tag{2-10}$$

In the MR community, the magnetic resonance data is usually not sparse in either its original domain (i.e., the image domain) or the domain that it is acquired (i.e., the Fourier domain). However, the magnetic resonance signal is sparse in some other transform domains. For instance, brain images are much sparser in the Wavelet domain than those in the image domain as depicted in Figure 2-4. The finite-differences sparsify angiograms well, as shown in Figure 2-5 [25]. The prior knowledge of transform sparsity can be incorporated, which leads to the following optimization problem

$$\hat{x} = \underset{x}{\text{argmin}} \quad \|F_{us}x - y\|_2^2 + \lambda\|\Psi x\|_1 \tag{2-11}$$

where x is the data in image domain; F_{us} is the undersampled Fourier operator; y is the observed k-space data from the MRI scanner; Ψ is a sparsifying transform; and λ is a regularization parameter. When the finite-differences are used as a sparsifying transform, it is referred to as Total Variation (TV).

2.3.3 Unconstrained Penalty Function Approximation Problem in MRSI

In MRSI, prior knowledge of the data could be exploited as well. A spectrum at each voxel is highly compressible in the frequency domain. Besides, metabolite maps extracted from the MRSI data at a specific range of frequencies are compressible in both the Wavelet domain and the finite-differences. Consequently, the regularized optimization problem can possibly be formulated as follows

$$\hat{x} = \underset{x}{\arg\min} \quad \|F_{us}x - y\|_2^2 + \lambda_S\|\Psi_{2D}x\|_1 + \lambda_{TV}TV_{3D}(x) \qquad (2\text{-}12)$$

where $x(x,y,f)$ is a data in the image domain; F_{us} is the undersampled 3D Fourier transform; $y(k_x, k_y, k_f)$ is the observed k-space data from the MRI scanner; λ_S and λ_{TV} are regularization parameters; Ψ_{2D} is an operator that applies the 2D Wavelet transform to the image at each frequency; and $TV_{3D}(.)$ is the total variation operators along three dimensions. The first terms $\|F_{us}x - y\|_2^2$ ensures that the reconstructed data is consistent with the observed data. The second term $\|\Psi_{2D}x\|_1$ imposes the transform sparsity constraint. The third term $TV_{3D}(x)$ enforces the smoothness of the data in the image domain. λ_S and λ_{TV} can be interpreted as relative costs of each constraint violation. Specifically, if λ_{TV} is relatively high as compared to λ_S, the reconstructed data tends to be very smooth in (x, y, f).

34
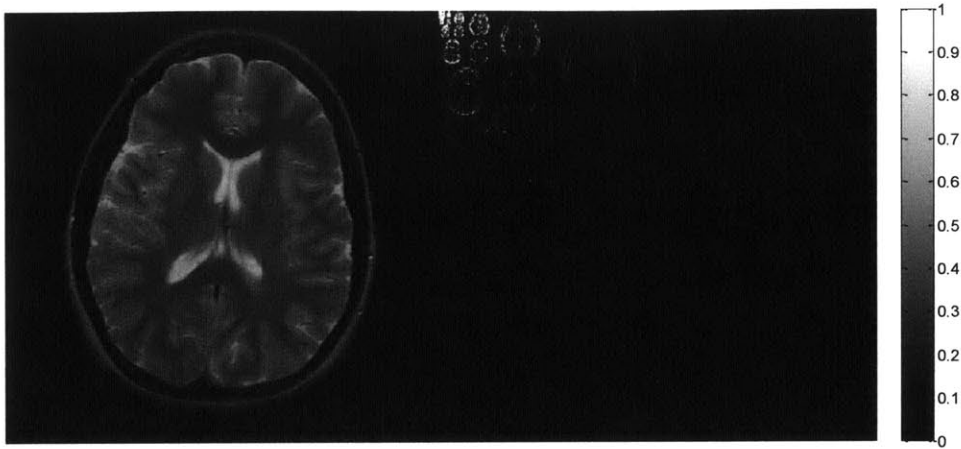
Figure 2-4: A brain data in the image domain (left) and in the Wavelet domain (right). The brain image is much sparser in the Wavelet domain than in the image domain. (Source: Lustig et al. [25]).
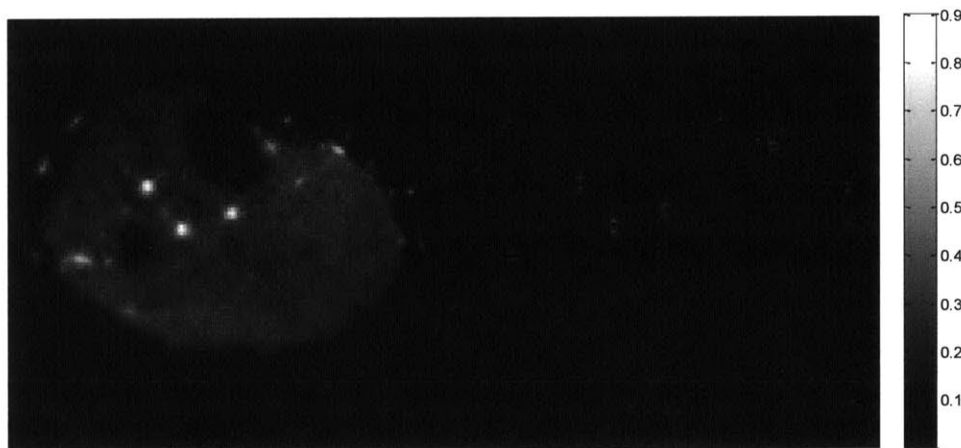
Figure 2-5: An angiogram of a leg in the image domain (left) and in the finite-differences domain (right). The finite-differences sparsify angiograms well. (Source: Lustig et al. [25]).

Chapter 3

Reconstruction of MRSI using Spectrum Modeling

While conventional magnetic resonance imaging provides structural information such as tissue boundaries, magnetic resonance spectroscopic imaging (MRSI) provides additional information on cellular activities at various spatial locations. This additional information is very useful to detect irregular changes of the metabolite concentration in specific brain regions, which indicate physiological abnormalities. While MRSI is clinically useful, it is very time-consuming to acquire the high-resolution MRSI data. In practice, the high resolution of the MRSI data is sacrificed in order to achieve the shorter acquisition time, so the resolution of typical MRSI data is very low. In order to estimate the relative intensities of metabolite signals at each voxel from the low-resolution MRSI data, model-based reconstruction methods have been proposed [2-4, 26, 32-37].

This chapter presents a two-step, model-based reconstruction method, which leads to an accurate reconstruction from the undersampled MRSI data. First, this method takes advantage of a fast water reference scan to estimate non-linear unknowns. Then, a regularized optimization problem with priors is formulated to reconstruct the MRSI data. As opposed to the methods proposed in [2, 26], which reconstruct the spectrum at each voxel separately, we reconstruct the spectra at all voxels simultaneously. This proposed reconstruction procedure allows us to incorporate the prior knowledge of the sparsity of metabolite maps in a transform domain into the optimization problem formulation. As a result, the metabolite maps can be more accurately recovered from the MRSI data.

Moreover, the acquisition time needed for this method is significantly less than that of the existing methods because the proposed method allows the undersampling of k-space measurements without sacrificing the image quality.

In this chapter, we first present a mathematical model for a typical magnetic resonance spectroscopic imaging spectrum. Then, the proposed reconstruction procedure is described in detail. Next, the performance of the proposed method is compared to that of the conventional least-squares method on the experimental data from a healthy human subject. The root-mean-square error is used as a criterion. Finally, conclusions about the proposed method are discussed.

3.1 Theory

3.1.1 Model Description

The magnetic resonance spectroscopic imaging spectrum $x(t)$ at each voxel over time can be expressed as a summation of K metabolite bases

$$x(t) = \sum_{k=1}^{K} a_k b_k(t) e^{j(\omega_k t + \phi_k)} \quad , t > 0 \tag{3-1}$$

where a_k is the amplitude corresponding to the basis for the kth metabolite, $b_k(t)$; ω_k is the frequency of the kth metabolite; ϕ_k is the phase of the kth metabolite; and K is the number of metabolites in the model. There are many choices for the metabolite basis. For instance, in Reference [2], the kth metabolite basis is chosen to be $e^{-\frac{t}{T_2^{(k)}}}$. As a result, the time signal $x(t)$ is expressed as a summation of K decaying exponentials

$$x(t) = \sum_{k=1}^{K} a_k e^{-\frac{t}{T_2^{(k)}}} e^{j(\omega_k t + \phi_k)} \quad , t > 0 \tag{3-2}$$

Let ω_0 and ϕ_0 be a reference frequency and a reference phase, respectively. Consider the kth metabolite with the corresponding frequency ω_k. The difference between ω_0 and ω_k can then be computed as follows

$$\Delta\omega_k = \omega_0 - \omega_k = \gamma B_0 - \gamma(1 - \sigma)B_0 = \gamma\sigma B_0.$$

38

In the presence of the B_0 inhomogeneity, the difference between two frequencies becomes

$$\Delta\omega_k = \omega_0 - \omega_k$$
$$= \gamma(B_0 + \Delta B_0) - \gamma(1 - \sigma)(B_0 + \Delta B_0)$$
$$= \gamma\sigma B_0 + \gamma\sigma\Delta B_0$$
$$\approx \gamma\sigma B_0.$$

Since $\gamma\sigma\Delta B_0 \ll \gamma\sigma B_0$, the change in the difference in frequencies due to the B_0 inhomogeneity is negligible. Thus, each ω_k in Equation (3-1) and (3-2) can be replaced by $\omega_0 - \Delta\omega_k$, even with the B_0 inhomogeneity. Similarly, ϕ_k can be replaced by $\phi_0 - \Delta\phi_k$. With this modification, the time signal becomes

$$x(t) = \sum_{k=1}^{K} a_k b_k(t) e^{j((\omega_0 - \Delta\omega_k)t + (\phi_0 - \Delta\phi_k))}. \tag{3-3}$$

The data obtained from the MRI scanner is equal to $x(t) + n(t)$, where $n(t)$ is approximately the white complex Gaussian noise. Figure 3-1 shows the Fourier transform of a synthetic metabolite signal in the time domain under the model described by Equation (3-3) with $K = 3$. This signal contains three metabolites, which are NAA, creatine, and choline.

3.1.2 Reconstruction

With the model described above, there are only a few unknowns to be determined. The underlying signal can easily be recovered in two steps.

First, the water reference data along with priori information is used to determine $\omega_0, \Delta\omega_k$, ϕ_0, $\Delta\phi_k$, and $b_k(t)$ in Equation (3-3). We then use these parameters to construct the matrix B, which contains the bases of the metabolites. Specifically, the kth column of B is $b_k(t)e^{j((\omega_0 - \Delta\omega_k)t + (\phi_0 - \Delta\phi_k))}$. In this chapter, we assume that the lineshape of the metabolites are the same as that of the water reference signal at the same spatial location. Mathematically, $b_k(t) = b(t), \forall_{k=1,...,K}$, where $b(t)$ is the basis obtained from the water reference signal at the same spatial location.

39

Second, the a_k's are recovered from the acquired data by solving a regularized optimization problem. There are multiple ways to set up the problem. The conventional method formulates it as the least-squares problem

$$\underset{a}{\text{minimize}} \quad \left\| a \right\|_2^2 \tag{3-4}$$

$$\text{subject to} \quad \left\| FBa - y \right\|_2^2 < \epsilon$$

where a is the vector containing a_k's; B contains the bases of metabolites in the model; y is the observed k-space data from the MRI scanner; F is the fully-sampled Fourier operator; and ϵ is a threshold for the observed data fidelity. This optimization problem can be solved quickly using the pseudoinverse [2, 26].

Although the conventional method yields fast and accurate reconstructions from the *fully-sampled* k-space data, it yields inaccurate reconstructions from the *undersampled* k-space data because the acquired data is contaminated by both aliasing and undersampling artifacts. To mitigate these contaminations, we formulate the optimization problem differently by incorporating the prior knowledge of the data structure. The proposed method solves the following unconstrained optimization problem using a nonlinear conjugate gradient descent algorithm with backtracking line search [25]:

$$\underset{a}{\text{minimize}} \left\| F_{us}Ba - y \right\|_2^2 + \lambda_{TV}TV(Ba) \tag{3-5}$$

where a is the vector containing a_k's; B contains the bases of metabolites; y is the observed k-space data from the MRI scanner; F_{us} is the undersampled Fourier operator; and $TV(.)$ is the total variation operator. Figure 3-2 shows an example of B that contains three metabolite bases.

As opposed to the algorithm used in [2, 3, 26], which solves for a at each voxel separately, we solve for a's at all voxels simultaneously. This approach allows us to impose the additional prior knowledge via a regularization term. Specifically, we include the total variation term in the formulation for two main reasons. First, the underlying spectra are sparse in the finite-differences domain. Second, the metabolite map obtained from the underlying signals is spatially smooth. By imposing the TV term, we narrow

down the search space, which leads to better reconstructions. With the proposed method, we reduce the acquisition time by undersampling the data in k-space, while the regularization term preserves the high reconstruction quality. Figure 3-3 shows a block diagram of the proposed method.

For the results shown in this chapter, we forced B and y to be real matrices by omitting the imaginary parts of these matrices. The reason is that the peaks of the spectra in the k-pace under this model (i.e., the peaks of FBa and y) become narrower when we restrict them to reside in the space of real numbers. With narrower peaks, a specific peak has fewer overlaps with other peaks, so we obtain better peak separations. To see this, consider a single peak with no delay between the excitation time and the acquisition time (i.e., the data collection starts exactly at $t = 0$). Then, using Equation (3-2), the data is modeled by

$$x(t) = \begin{cases} a_1 e^{-\frac{t}{T_2^{(1)}}} e^{j\omega_1 t} & , t \geq 0 \\ 0 & , t < 0 \end{cases}$$

If we take the Fourier transform of $x(t)$, then we obtain

$$X(\omega) = \mathcal{F}\{a_1 e^{-\frac{t}{T_2^{(1)}}} e^{j\omega_1 t} u(t)\}$$

$$= \left(\frac{1}{2\pi} \mathcal{F}\{a_1 \times e^{j\omega_1 t}\} * \mathcal{F}\left\{e^{-\frac{t}{T_2^{(1)}}} u(t)\right\}\right)$$

$$= \frac{1}{2\pi}\left(2\pi a_1 \delta(\omega - \omega_1)\right) * \left(\frac{1}{\frac{1}{T_2^{(1)}} + j\omega}\right)$$

$$= \frac{a_1}{\frac{1}{T_2^{(1)}} + j(\omega - \omega_1)}$$

$$= \frac{a_1\left(\frac{1}{T_2^{(1)}} - j(\omega - \omega_1)\right)}{\frac{1}{\left(T_2^{(1)}\right)^2} + (\omega - \omega_1)^2}$$

$$= \frac{a_1\left(T_2^{(1)} - j\left(T_2^{(1)}\right)^2 (\omega - \omega_1)\right)}{1 + \left(T_2^{(1)}(\omega - \omega_1)\right)^2}$$

$$= \frac{a_1 T_2^{(1)} - j a_1 \left(T_2^{(1)}\right)^2 (\omega - \omega_1)}{1 + \left(T_2^{(1)}(\omega - \omega_1)\right)^2}$$

$$= \frac{a_1 T_2^{(1)}}{1 + \left(T_2^{(1)}(\omega - \omega_1)\right)^2} - j\frac{a_1 \left(T_2^{(1)}\right)^2 (\omega - \omega_1)}{1 + \left(T_2^{(1)}(\omega - \omega_1)\right)^2}$$

$$Re\{X(\omega)\} = \frac{a_1 T_2^{(1)}}{1 + \left(T_2^{(1)}(\omega - \omega_1)\right)^2}$$

$$Im\{X(\omega)\} = \frac{-a_1 \left(T_2^{(1)}\right)^2 (\omega - \omega_1)}{1 + \left(T_2^{(1)}(\omega - \omega_1)\right)^2}$$

$$|X(\omega)| = \frac{a_1 T_2^{(1)} \left(1 + \left(T_2^{(1)}\right)^2 (\omega - \omega_1)^2\right)^{\frac{1}{2}}}{1 + \left(T_2^{(1)}(\omega - \omega_1)\right)^2}$$

where $X(\omega)$ is the Fourier transform of $x(t)$ at different frequencies ω; $Re\{X(\omega)\}$ is the real part of $X(\omega)$; $Im\{X(\omega)\}$ is the imaginary part of $X(\omega)$; $|X(\omega)|$ is the magnitude of $X(\omega)$; $u(t)$ is a unit step function; and $\mathcal{F}\{.\}$ is the Fourier transform operator. The real part of $X(\omega)$ decays at a rate of $\frac{1}{\omega^2}$, whereas the imaginary part and the magnitude of $X(\omega)$ decay at a rate of $\frac{1}{\omega}$. Thus, the peaks of a signal plot of $Re\{X(\omega)\}$ will be narrower than those of $Im\{X(\omega)\}$ and $|X(\omega)|$. Figure 3-4 shows the real part, imaginary part, and magnitude of creatine and choline bases from top to bottom, respectively. Similarly, Figure 3-5 presents the real part, imaginary part, and magnitude of the summation of creatine and choline bases. As expected, it is easier to distinguish the creatine and choline peaks by examining the plot of the real part of the combined signal.
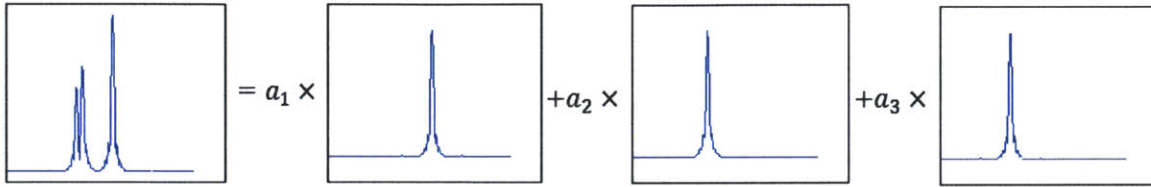
Figure 3-1: The Fourier transform of a synthetic metabolite signal in the time domain under the model described by Equation (3-3) with $K = 3$. This signal contains three metabolites, which are NAA, creatine, and choline.
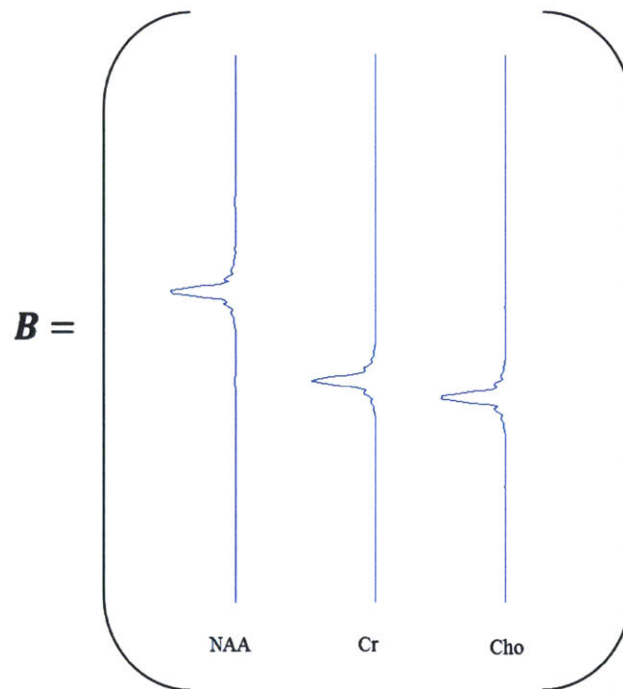
Figure 3-2: An example of B, which contains three metabolite bases: NAA, creatine, and choline.
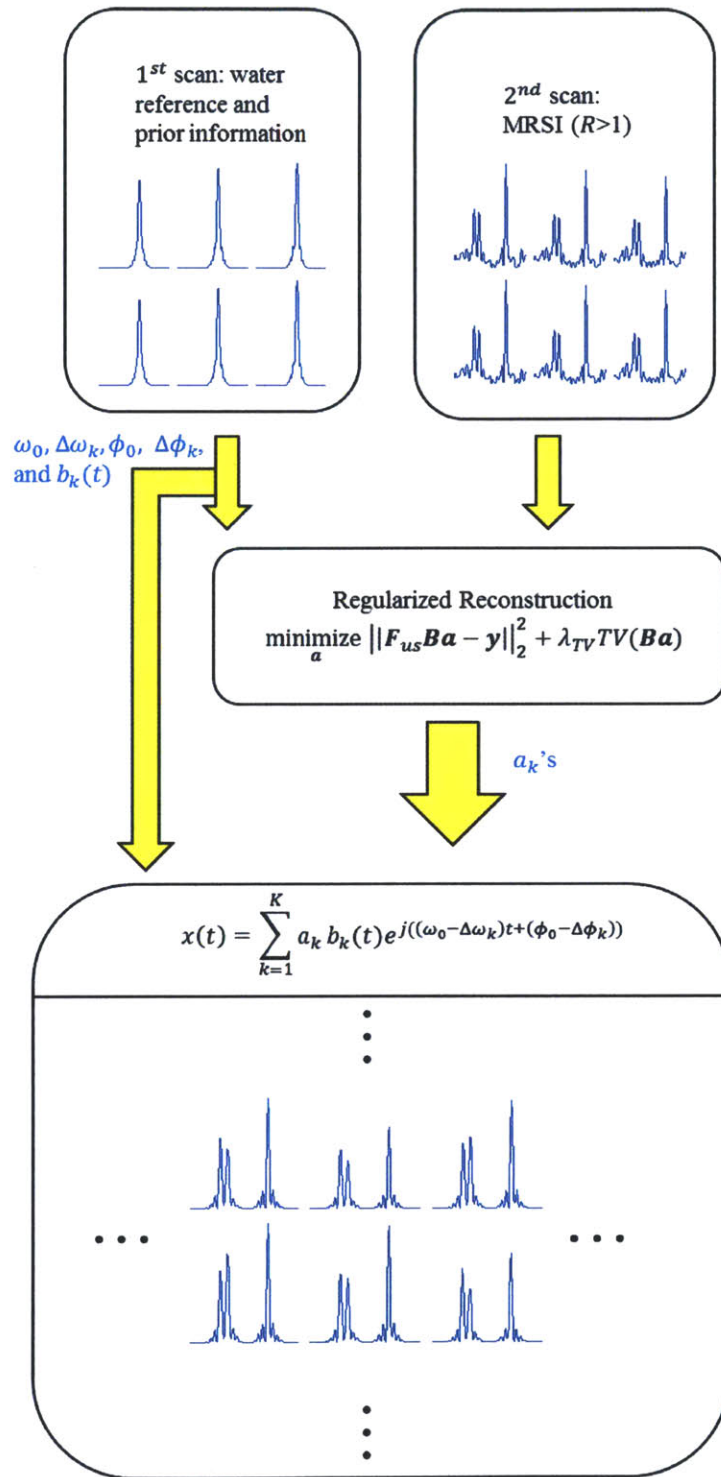
Figure 3-3: A block diagram of the proposed two-step, model-based reconstruction method.
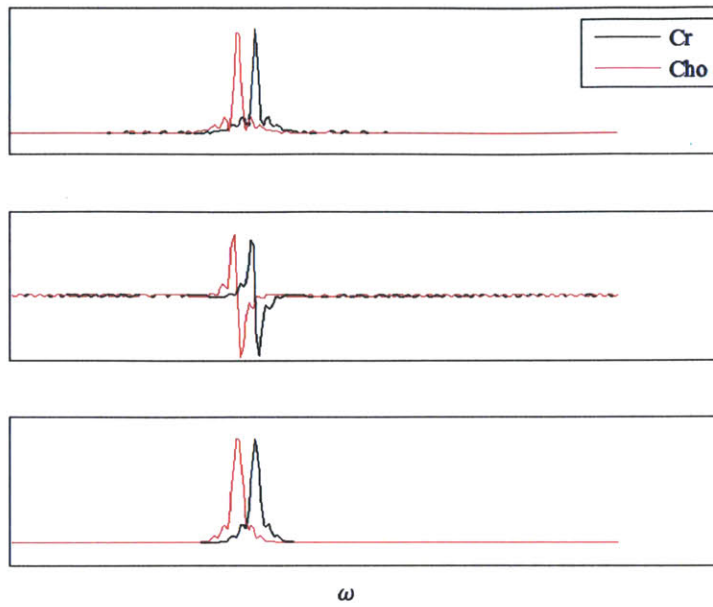
Figure 3-4: The real part, imaginary part, and magnitude of the synthetic creatine (black) and choline basis (red) from top to bottom, respectively.
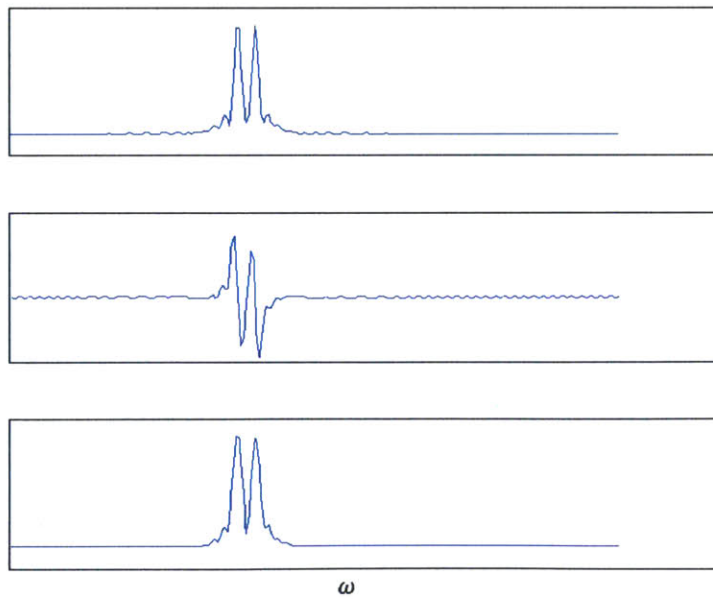
Figure 3-5: The real part, imaginary part, and magnitude of the summation of creatine and choline bases. The real part of the combined signal establishes the better separation between the creatine and choline peaks.

3.2 Methods

In this section, we assessed the performance of the proposed method using experimental data from a healthy human subject. The magnetic resonance spectroscopic imaging data set were fully sampled with a resolution of 1.1 cubic centimeters at 1.5 Tesla using spiral trajectories and gridding algorithms. The echo time (TE) and repetition time (TR) were 144 and 2000 milliseconds, respectively. The total scan times were 15 minutes and 20 seconds. We used spin-echo spectral-spatial pulses to suppress the water resonance. In addition, we used inversion recovery with the inversion time (TI) of 170 milliseconds to suppress the lipid resonance. After that, we manually removed the remaining lipid resonances from the post-gridded MRSI data set and retrospectively undersampled the resulting data in MATLAB.

Figure 3-6 shows an example of the undersampling patterns at acceleration factors of two ($R = 2$) and six ($R = 6$) for a specific time point. The k-space data is sampled more densely in the middle due to its high energy at these locations. For the results shown in the next section, we used the same undersampling pattern for all time points. Note that the proposed method also works well when different undersampling patterns are used at different time points.

We used the proposed method to reconstruct the MRSI spectra from undersampled k-space measurements with various acceleration factors R ranging from two to six. The number of metabolites K was chosen to be three to represent NAA, creatine, and choline. Consequently, we can construct the NAA, creatine, and choline maps from the reconstructed MRSI spectra. The results were quantitatively compared to those obtained from the least-squares method with the same undersampling pattern and acceleration factors. As opposed to the proposed algorithm, the conventional least-squares method does not impose any prior information on the reconstruction process. In this experiment, we compared the performance of the proposed method to that of the conventional method using the root-mean-square error (RMSE) of the reconstructed metabolite map as a criterion. The RMSE of each method was computed with respect to the ground truth as follows

$$RMSE = 100 \times \frac{\|\hat{x} - x\|_2}{\|x\|_2}$$

where x is the ground truth, and $\hat{x}$ is the reconstructed metabolite map from each method. The reconstructed metabolite map from the fully-sampled least-squares reconstruction ($R = 1$) was used as the ground truth.

Undersampling pattern $(R = 2)$
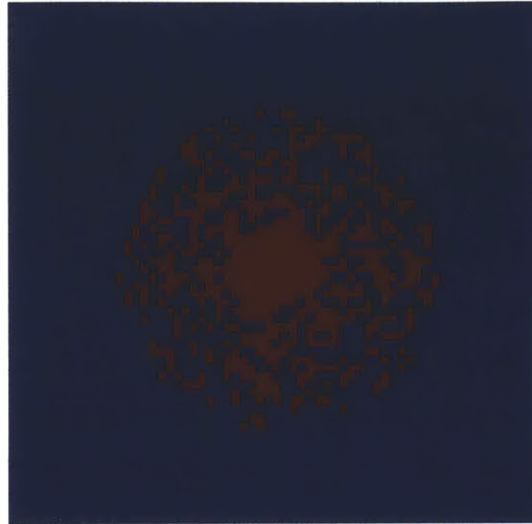
Undersampling pattern $(R = 6)$

Figure 3-6: Undersampling patterns at acceleration factors of two (top) and six (bottom) for a specific time point. The k-space locations obtained are indicated in red. The k-space data is sampled more densely in the middle due to its high energy at these locations.

3.3 Results and Discussion

The RMSEs of the reconstructed NAA, creatine, and choline maps obtained from the conventional LS method and the proposed method at various acceleration factors ranging from two to six are shown in Figure 3-7, Figure 3-8, and Figure 3-9, respectively. As shown in Figure 3-7, at $R = (2, 3, 4, 5, 6)$, the proposed method yielded approximately (1.81, 2.24, 2.63, 3.33, 4.18)% RMSE for the NAA reconstruction compared to (3.73, 5.46, 7.99, 6.85, 8.01)% RMSE obtained from the conventional LS method. By incorporating the prior knowledge into the optimization problem, the RMSEs of the reconstructed NAA maps were reduced by approximately two to three times. As shown in Figure 3-8, at $R = (2, 3, 4, 5, 6)$, the proposed method yielded approximately (2.26, 3.77, 4.32, 4.17, 4.59)% RMSE for the creatine reconstruction compared to (4.86, 6.33, 9.28, 8.27, 9.59)% RMSE obtained from the conventional LS method. The proposed method reduced the RMSEs of the reconstructed creatine maps by approximately two times. As shown in Figure 3-9, at $R = (2, 3, 4, 5, 6)$, the proposed method yielded approximately (2.46, 2.96, 3.41, 4.36, 5.93)% RMSE for the choline reconstruction compared to (4.35, 5.73, 7.34, 6.78, 7.52)% RMSE obtained from the conventional LS method. The proposed method reduced the RMSEs of the reconstructed choline maps by approximately 1.3 to 2 times.

For the purpose of visualizations, Figure 3-10, Figure 3-11, Figure 3-12, and Figure 3-13 focus on the case when R is equal to two and six. Figure 3-10 shows the reconstructed NAA, creatine, and choline maps from the undersampled MRSI data ($R = 2$) from left to right with the corresponding RMSE in the upper right hand corner. The reconstructed map from the fully-sampled LS method ($R = 1$), proposed method ($R = 2$), and conventional LS method ($R = 2$), were presented from the top to bottom rows. Figure 3-11 presents a bar plot, which explicitly compares the RMSEs of the reconstructed metabolite maps obtained from the LS method to those obtained from the proposed method at an acceleration factor of two. The proposed method reconstructed the NAA, creatine, and choline maps with corresponding RMSEs of 1.81%, 2.26%, and 2.46%, respectively, whereas the conventional LS method reconstructed the NAA, creatine, and choline maps with corresponding RMSE of 3.73%, 4.86%, and 4.35%,

respectively. The proposed method gave approximately two times lower RMSEs, compared to those obtained from the conventional LS method.

Figure 3-12 shows the spectra from voxels inside the red box that was placed on top of the water image. The fully-sampled observed spectra, reconstructed spectra obtained from the conventional LS method at $R = 1$, and reconstructed spectra obtained from the proposed method at $R = 2$ were shown in red, green, and blue, respectively. The differences between the ground truth and reconstructed spectra from the proposed method were shown in magenta. Because the background noise and other small metabolites were not modeled in Equation (3-3), both the conventional LS and proposed methods produce the solution that did not contain these elements as reflected in the distinction between the observed spectra (shown in red) and the reconstructed spectra (shown in blue and green). The distinction is more noticeable in the frequency ranges in which NAA, creatine, and choline peaks do not reside.

Figure 3-13 shows the reconstructed NAA, creatine, and choline maps from the undersampled MRSI data ($R = 6$) from left to right with the corresponding RMSE in the upper right hand corner. The reconstructed maps from the fully-sampled LS method ($R = 1$), proposed method ($R = 6$), and conventional LS method ($R = 6$), were presented from the top to bottom rows. The proposed method reconstructed the NAA, creatine, and choline maps with corresponding RMSEs of 4.18%, 4.59%, and 5.93%, respectively, whereas the conventional LS method reconstructed the NAA, creatine, and choline maps with corresponding RMSE of 8.01%, 9.59%, and 7.52%, respectively. The proposed method gave approximately two times lower RMSEs of the reconstructed NAA and creatine maps, compared to those obtained from the conventional LS method. The RMSE of the reconstructed choline map was reduced by approximately 1.3 times using the proposed method.

As shown in Figure 3-10 and Figure 3-13, the proposed method yielded better reconstruction quality as indicated by both the lower RMSEs and the more similar spatial characteristics of the reconstructed metabolite maps to those of the ground truths. Because the conventional LS method reconstructs the spectrum at each voxel separately, it imposes no spatial constraints on the reconstructed metabolite maps. In other words, it

51

ignores the correlation between adjacent voxels. As a result, the conventional LS method cannot capture such small details as changes between the adjacent voxels of the metabolite maps, as shown in Figure 3-13. In contrast, by reconstructing the spectra at all voxels simultaneously, the proposed method can incorporate the prior knowledge of the metabolite map into the reconstruction process. Specifically, the proposed method enforces the prior knowledge through the total variation term. This regularization term restricts the search space to a set that contains only spatially-smooth solutions. Because we use the total variation operator as opposed to the l_2 smoothing operator, sharp edges in the underlying metabolite maps are not severely penalized and, hence, are preserved. This choice of a smoothing operator prevents our algorithm from providing a too-smooth solution. As shown in Figure 3-13, the spatial details of the reconstructed metabolite maps obtained from the proposed method are preserved.

In summary, although the data in k-space is undersampled, the proposed algorithm still yielded the accurate reconstruction because of two main factors. First, we do not fit the noise and unwanted metabolites in the reconstruction process by excluding the bases for these components from our model. Second, we impose the additional prior knowledge via the total variation term by solving the a's at all voxels simultaneously. Because the prior knowledge helps mitigate the undersampling artifacts, the proposed method yielded the reconstructions that are more accurate than those using the conventional method (about two times reduction in RMSE with R ranging from two to six).
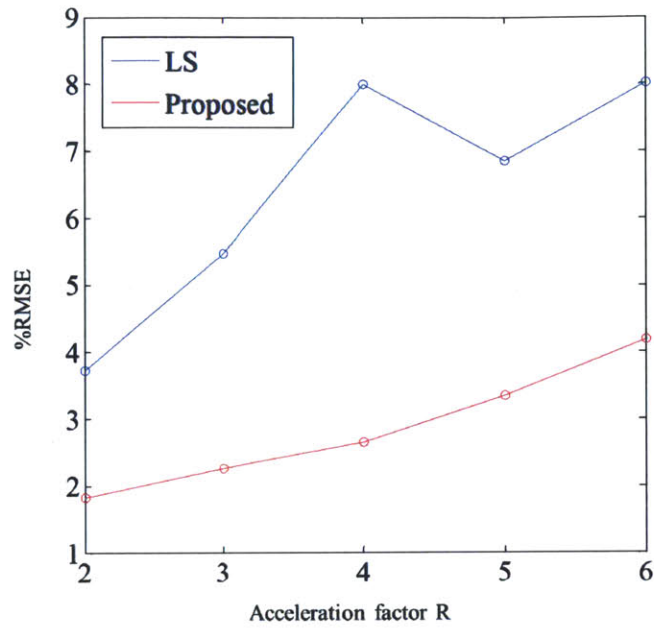
Figure 3-7: %RMSE of the reconstructed NAA map obtained from the conventional LS method (blue) and the proposed method (red) at various acceleration factors ranging from two to six.
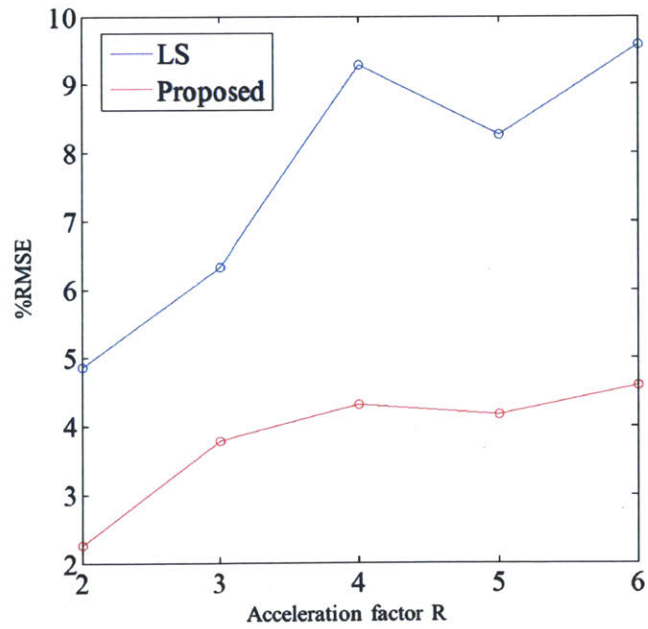
Figure 3-8: %RMSE of the reconstructed creatine map obtained from the conventional LS method (blue) and the proposed method (red) at various acceleration factors ranging from two to six.

53
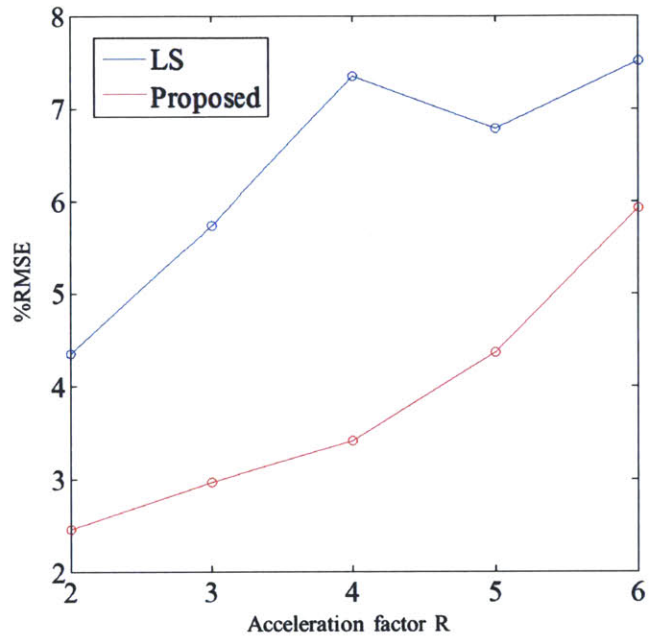
Figure 3-9: %RMSE of the reconstructed choline map obtained from the conventional LS method (blue) and the proposed method (red) at various acceleration factors ranging from two to six.
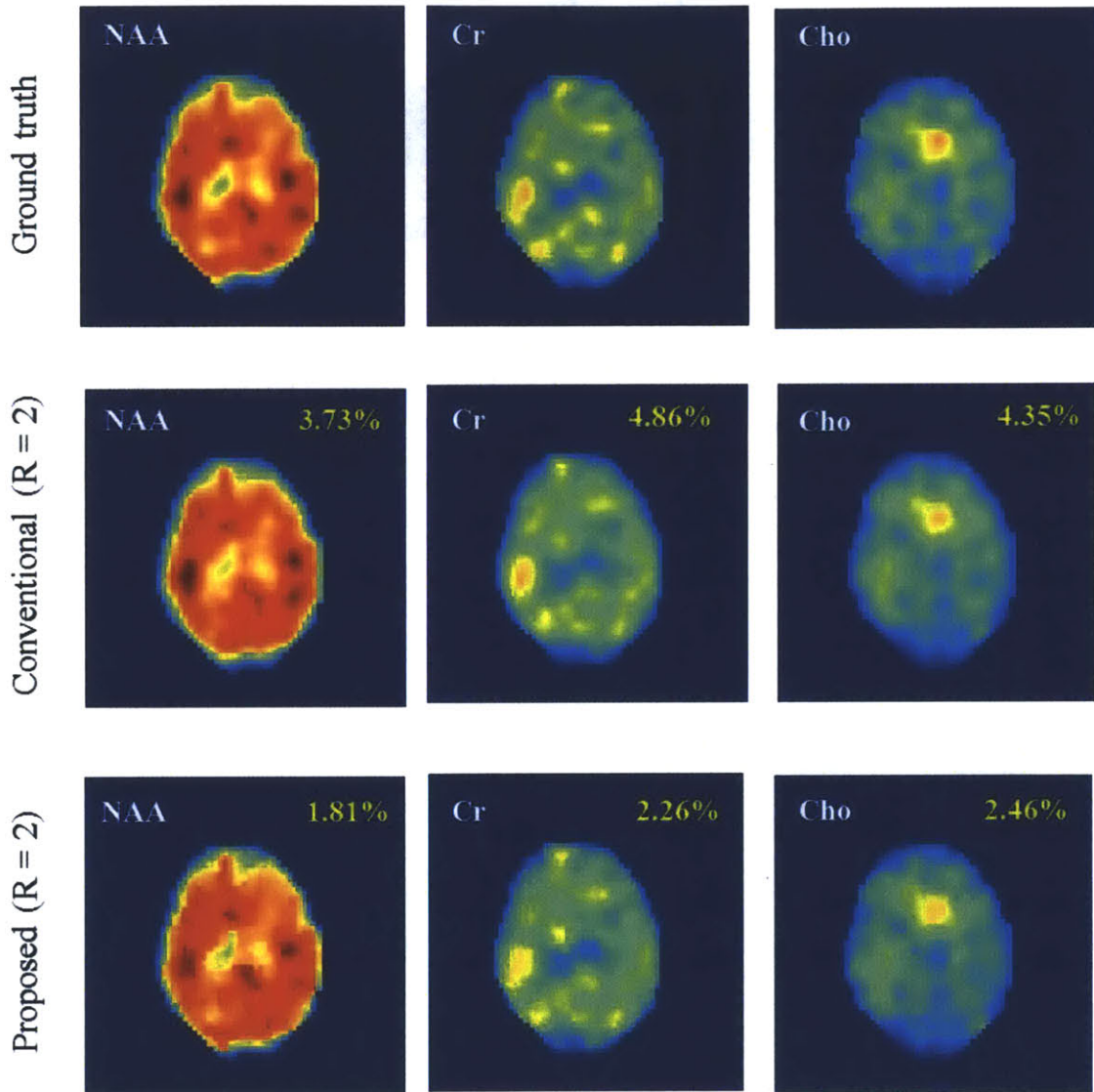
Figure 3-10: The reconstructed NAA (left column), creatine (middle column), and choline maps (right column) with the corresponding RMSE in the upper right hand corner. The reconstructed map from the LS method ($R = 1$), the proposed method ($R = 2$), and the LS method ($R = 2$) are shown in top, middle, and bottom rows, respectively.
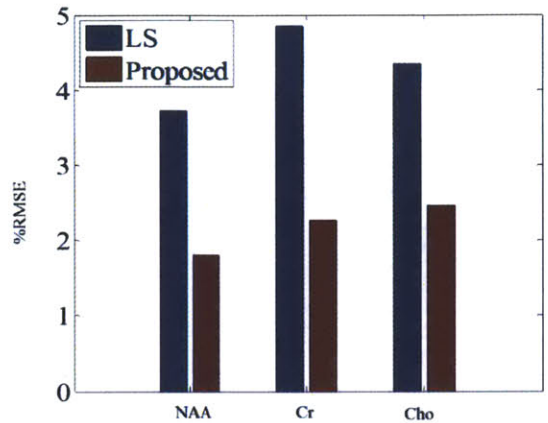
Figure 3-11: The RMSE comparison of the reconstructed metabolite map obtained from the LS method and the proposed method at an acceleration factor of two.
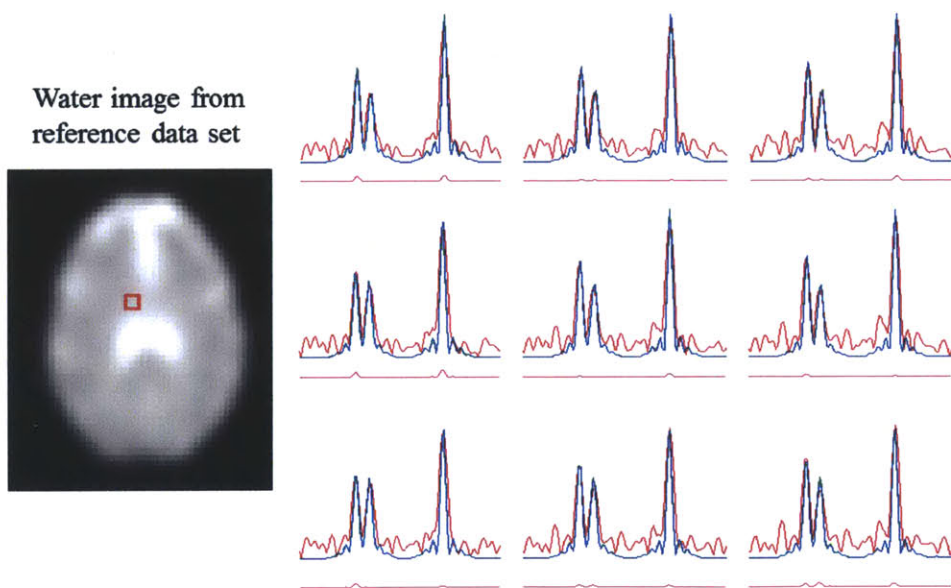
Figure 3-12: The spectra from voxels inside the red box that was placed on top of the water image. The fully-sampled observed spectra, reconstructed spectra obtained from the conventional LS method at $R = 1$, and reconstructed spectra obtained from the proposed method at $R = 2$ were shown in red, green, and blue, respectively. The differences between the ground truth and the spectra from the proposed method were shown in magenta.

56
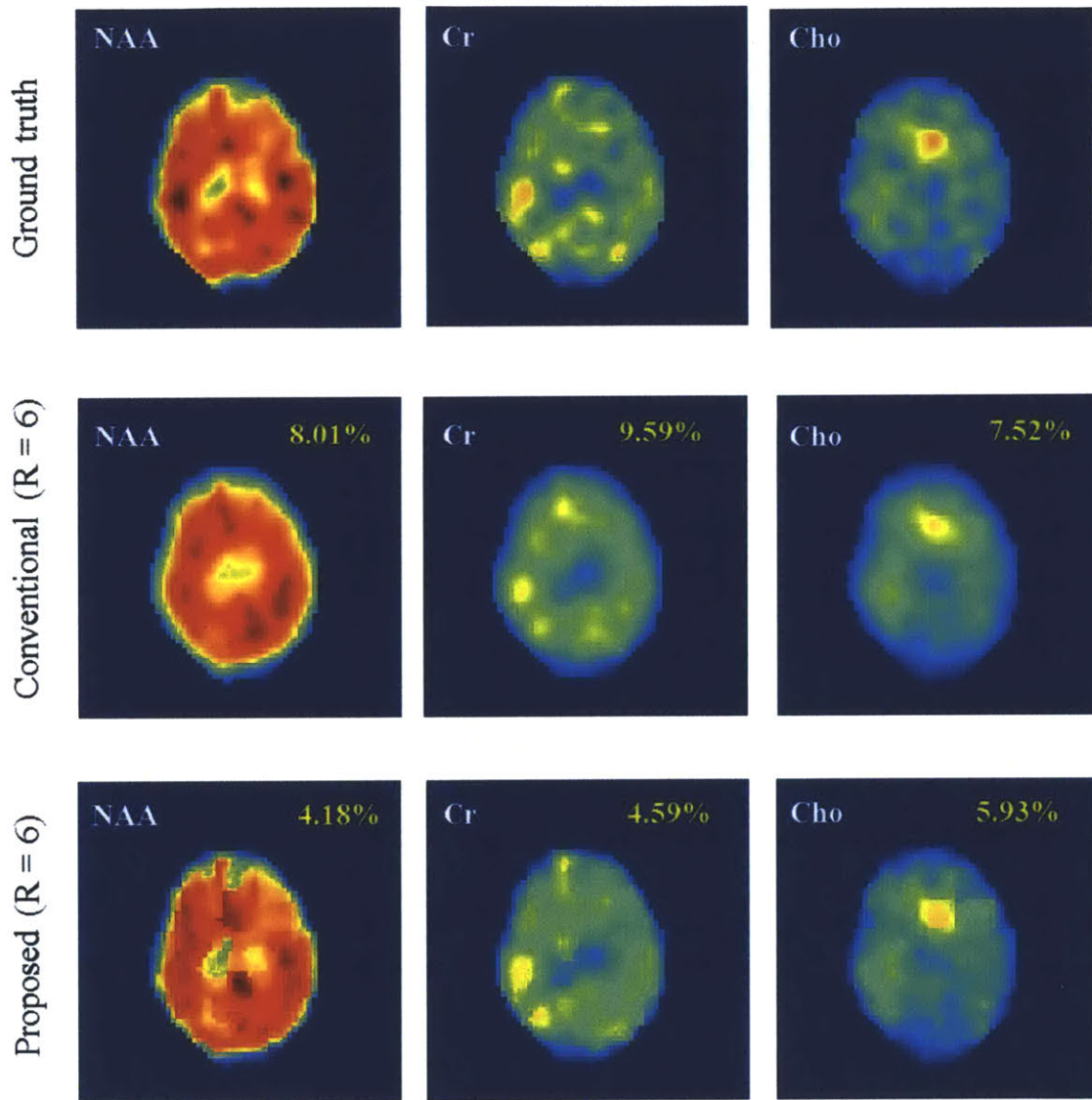
Figure 3-13: The reconstructed NAA (left column), creatine (middle column), and choline maps (right column) with the corresponding RMSE in the upper right hand corner. The reconstructed map from the LS method ($R = 1$), the proposed method ($R = 6$), and the LS method ($R = 6$) are shown in top, middle, and bottom rows, respectively.

3.4 Conclusion

By representing a time signal at each voxel as a summation of the individual metabolite basis and taking advantage of a quick water reference scan, there are only a few linear unknowns left to be determined. This allows us to undersample the magnetic resonance spectroscopic imaging data, which mitigates the limitation on long acquisition times. For the reconstruction process, we exclude the bases for the noise and unwanted metabolites from our model in order to eliminate these components from the reconstructed MRSI data. Furthermore, we incorporate the prior knowledge of the structure of the data into the optimization problem formulation through regularization in order to tackle the undersampling artifacts. The proposed method improves the reconstruction accuracy compared to that without regularization.

Chapter 4

Reconstruction of MRSI using N-Compartment Model

The combination of a segmented structural image and *fully-sampled* spectroscopic imaging data has been used to estimate metabolite values at each voxel. As described in [3, 22-24], the tissue boundaries (i.e., binary masks) are extracted from the segmented structural image. These methods assume that the metabolite values within the same tissue type are equal. However, a real human brain does not have this characteristic. To refine and improve these methods, this chapter presents an N-compartment-model reconstruction method with orthogonal polynomial masks. The proposed method allows the metabolite values within the same tissue type to vary by using more than one orthogonal polynomial masks instead of the single binary mask per compartment. In addition, the proposed method imposes the prior knowledge of the sparsity of the metabolite map in a transform domain. As a result, metabolite maps could be more accurately recovered from *undersampled* MRSI data. Because the proposed method allows the undersampling of k-space measurements, the acquisition time needed is significantly less than that of the existing methods.

In this chapter, we first present a conventional mathematical model and proposed mathematical model for the metabolite maps. The relationship and interpretation between these two models are then explained. Next, the reconstruction procedure is described in detail. Finally, the performance of the proposed method is compared to that of the conventional method on two data sets, which consist of a numerical magnetic resonance spectroscopic imaging phantom and in vivo acquisitions, using the RMSE as a criterion.

4.1 Theory

4.1.1 Model Description

Each high-resolution metabolite map is expressed as a superposition of N compartments

$$x = \sum_{k=1}^{N} m_k c_k \qquad (4\text{-}1)$$

where x is the metabolite map; m_k is the mask of the kth compartment; c_k is the scaling factor of the kth compartment; and N represents a number of compartments in consideration [3, 22-24]. This model assumes that metabolite values are constant within the same compartment. Figure 4-1 shows a high-resolution synthetic metabolite map that is expressed as a superposition of N compartments using Equation (4-1) with $N = 9$. However, the assumption that the metabolite values are constant within the same compartment is too strong as evidenced in real human brains. In fact, the metabolite values are slowly-varying within the same compartment.

The proposed method relaxes the previously mentioned, strong assumption. Specifically, the proposed method assumes that the metabolite values within the same tissue type vary instead of being constant. With this new assumption, the existing model is extended to accommodate more than one mask per compartment. Consequently, each high-resolution metabolite map is expressed as

$$x = \sum_{k=1}^{N} \sum_{l=1}^{L} m_{kl} c_{kl} \qquad (4\text{-}2)$$

where m_{kl} is the lth mask of the kth compartment; c_{kl} is the lth scaling factor of the kth compartment; N is a number of compartments in consideration; and L is a number of different masks for each compartment. Figure 4-2 shows a high-resolution synthetic metabolite map under this modified model with $N = 9$ and $L = 3$. Here, three masks are used to represent each compartment.

The proposed model can simply be extended from the old model by generating $L - 1$ additional masks for each compartment based on a polynomial expansion. Specifically, for a specific compartment, each mask corresponds to each term of a

60

polynomial. For instance, when the 0th order polynomial is used (i.e., $L = 1$), the new model is simplified to the old model because the 0th order term of the polynomial is just the constant term. When the first order polynomial mask is used (i.e., $L = 3$), we have $m_{11} = m_1, m_{12} = m_1 \otimes |x_{variation}|$, and $m_{13} = m_1 \otimes |y_{variation}|$ where m_1 is the mask of the 1st compartment in the model described by Equation (4-1); m_{1l} is the lth mask of the 1st compartment in the model described by Equation (4-2); $\otimes$ is an element-wise multiplication operator; and $x_{variation}$ and $y_{variation}$ are normalized spatial variation along the x-axis and y-axis, respectively. Figure 4-3 demonstrates the case when the first order polynomial is used (i.e., $L = 3$). Two additional masks for each compartment are generated based on the expansion of the 1st order polynomial. Here, three masks are used to describe each compartment. The first mask corresponds to the 0th order term. The second mask captures the first order variation along the x-direction. Similarly, the third mask captures the first order variation along the y-direction. The weighted combination of these three masks allows smooth changes of metabolite values of adjacent voxels within the same compartment. Note that the low polynomial order leads to the model that allows the metabolite values to change slowly within the same tissue type, while the high polynomial order allows the metabolite values to change abruptly within the same tissue type.

By generating the masks based on this type of polynomial, they are not orthogonal to each other. There exist many ways to transform such masks so that they become orthogonal to each other. One way to achieve such a task is to apply the Gram-Schmidt process [38]. However, this method does not preserve the original structure of the masks. In other words, the resulting masks generated by the Gram-Schmidt process lose their original structures and, hence, their physical meaning. Alternatively, the new orthogonal masks could be obtained from the existing masks by finding the nearest orthogonal matrix as measured by the Frobenius norm. This can be done easily using the singular value decomposition (SVD) as described in Algorithm 1 [39]. Figure 4-4 shows the resulting orthogonal masks that were generated by applying Algorithm 1 to all masks of the 1st compartment.

4.1.2 Reconstruction

Two sets of data are collected at the same orientation: the high-resolution structural images and low-resolution MRSI data. We obtain the tissue boundaries from the high-resolution structural images using the automatic segmentation programs. The binary mask m_k (i.e., the mask for the kth compartment of the model described by Equation (4-1)) is then extracted from each compartment of the segmented structural images. After that, we generate L orthogonal masks $m_{kl}^\perp$'s for the kth compartment from each m_k using the steps described in the previous section. We window each mask $m_{kl}^\perp$ in k-space to match the resolution of the acquired MRSI data. The resulting low-resolution masks are vectorized and then stacked into a single matrix $M^{(low)}$. Finally, the relative intensities of metabolite signals are estimated by solving an optimization problem. A flow chart representing the complete procedures is given in Figure 4-5.

There are many ways to set up the optimization problem. The conventional method is to formulate it as the least-squares solution

$$\underset{c}{\text{minimize}} \ \left\| FM^{(low)}c - y \right\|_2^2 \tag{4-3}$$

where $M^{(low)}$ is the matrix that contains the low-resolution masks; c is the vector that stores estimated metabolite values; y is the observed low-resolution data in k-space; and F is the fully-sampled Fourier transform. The problem presented in Equation (4-3) can be easily solved using the pseudo-inverse [3, 22, 24].

In this work, we formulated an optimization problem differently so that we could simultaneously enforce the prior knowledge about tissue boundaries, slowly-varying nature of the metabolite values, and sparsity of the metabolite map in a transform domain. By including these priors in the formulation, the undersampling data in k-space is possible. To estimate the metabolite values, we solve the following optimization problem using a nonlinear conjugate gradient descent algorithm with backtracking line search [25]

$$\underset{c}{\text{minimize}} \ \left\| F_{us}M^{(low)}c - y \right\|_2^2 + \lambda_s \left\| \psi M^{(low)}c \right\|_1 \tag{4-4}$$

where $M^{(low)}$ is the matrix that contains the low-resolution masks; c is the vector that stores estimated metabolite values; y is the observed low-resolution data in k-space; F_{us}

is the undersampled Fourier transform; ψ is the sparsifying transform; and λ_S is a regularization parameter. The first terms $\left\|F_{us}M^{(low)}c - y\right\|_2^2$ ensures that the reconstructed data is consistent with the observed data. The second term $\left\|\psi M^{(low)}c\right\|_1$ imposes the transform sparsity constraint. The regularization parameter λ_S can be interpreted as the relative cost of each constraint violation.

We also set up the following optimization problems

$$\underset{c}{\text{minimize}} \;\; \left\|F_{us}M^{(low)}c - y\right\|_2^2 + \lambda_S \left\|\psi M^{(low)}c\right\|_1 + \lambda_{TV}TV(M^{(low)}c) \qquad (4\text{-}5)$$

and

$$\underset{c}{\text{minimize}} \;\; \left\|F_{us}M^{(low)}c - y\right\|_2^2 + \lambda_S \left\|\psi M^{(low)}c\right\|_1 + \lambda_{TV}TV(c) \qquad (4\text{-}6)$$

where $M^{(low)}$ is the matrix that contains the low-resolution masks; c is the vector that stores estimated metabolite values; y is the observed low-resolution data in k-space; F_{us} is the undersampled Fourier transform; ψ is the sparsifying transform; $TV(.)$ is the total variation operator; and λ_S and λ_{TV} are regularization parameters. Although these two methods yield reconstruction results that are comparable to that of the proposed method, the algorithms are much slower than the proposed method because they compute finite-differences at every iteration. As a result, the proposed method is preferable.
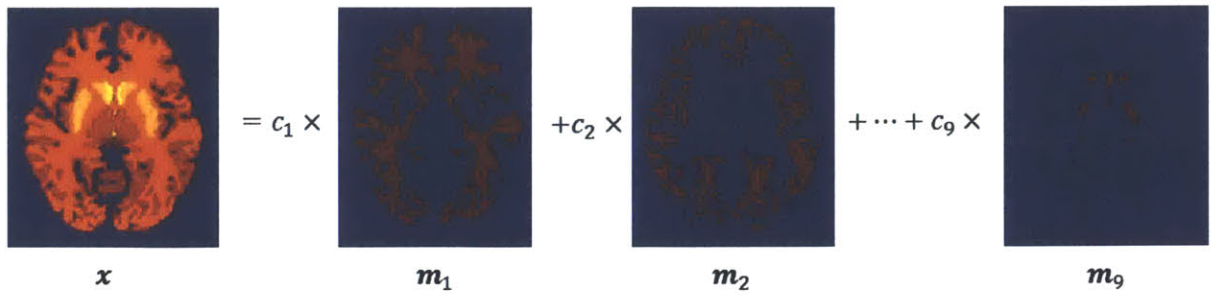
Figure 4-1: A high-resolution synthetic metabolite map is expressed as a superposition of N compartments using Equation (4-1) with $N = 9$.
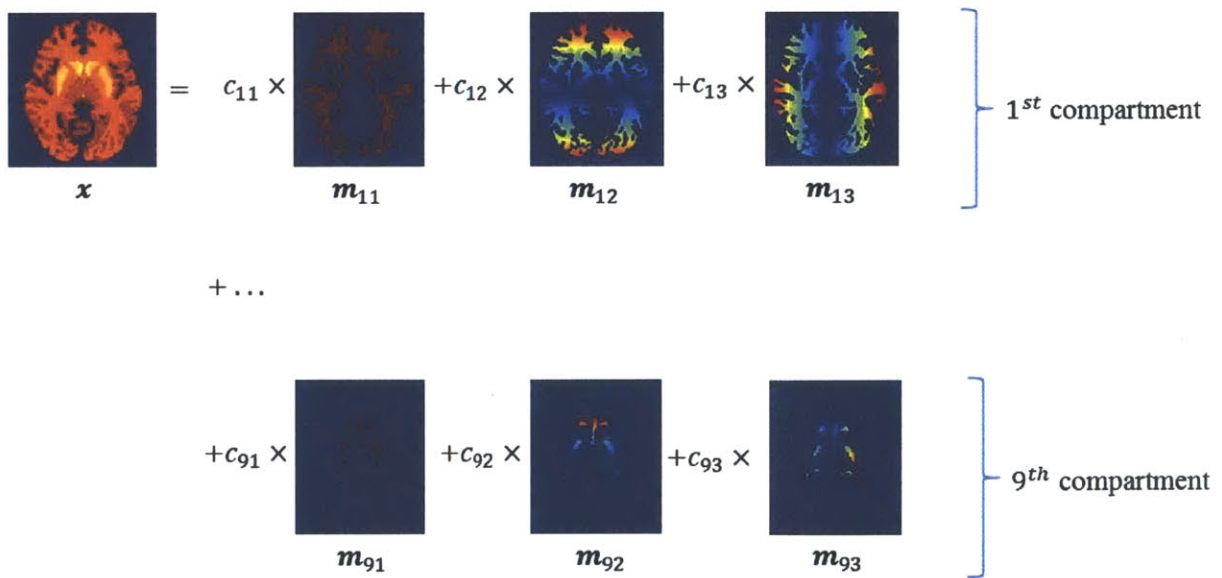
Figure 4-2: A high-resolution synthetic metabolite map under the model described in Equation (4-2) with $N = 9$ and $L = 3$. Three masks are used to represent each compartment.
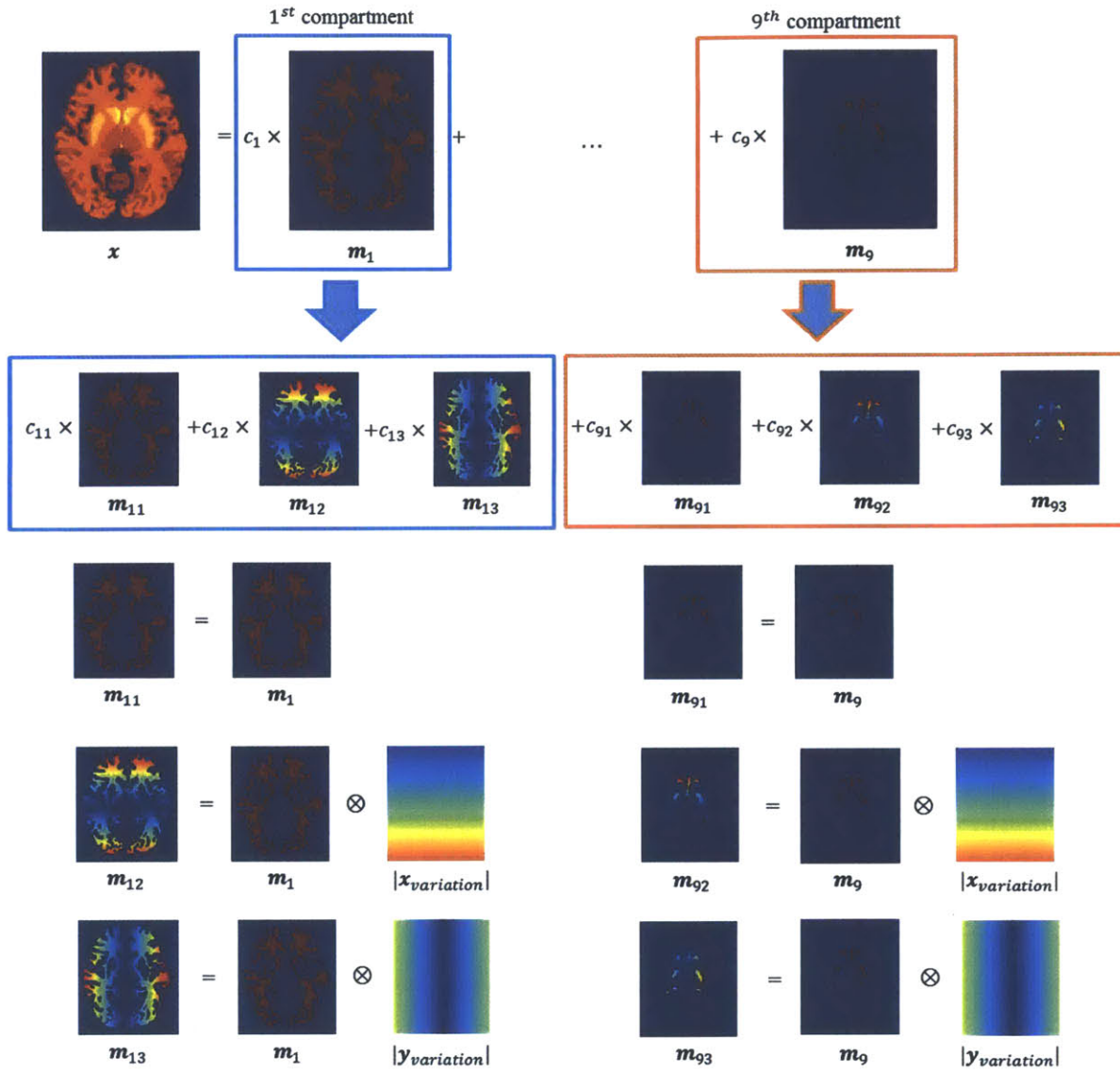
Figure 4-3: Additional $L-1$ masks for each compartment are generated based on the expansion of the 1st order polynomial. Here, we have three masks ($L=3$) for each of the nine compartments ($N=9$). The first mask corresponds to the 0th order term. The second mask captures the first order variation along the x-direction. The third mask captures the first order variation along the y-direction.

Algorithm 1: The nearest orthogonal bases as measured by the Frobenius norm were generated from the existing bases in a complex Hilbert space. The orthogonal bases were obtained by solving the least-squares inner product shaping problem using the singular value decomposition (SVD).

Algorithm 1 Solving the least-squares inner product shaping problem using the SVD
For each compartment k,   1. Create a matrix M_k by stacking each mask m_{kl} into each column of M_k for $l = 1, 2, \ldots, L$ 2. Decompose M_k using the singular value decomposition (SVD): $M_k = U\Sigma V^H$ 3. $M_k \leftarrow UV^H$ 4. Columns of the modified matrix M_k are the resulting orthogonal masks
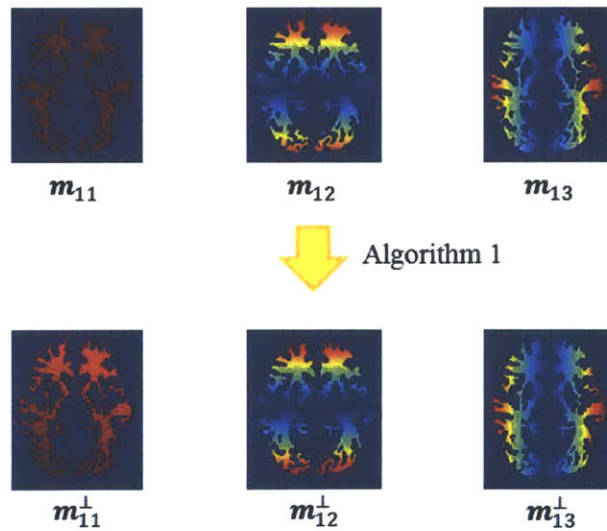
Figure 4-4: The resulting orthogonal masks generated by applying Algorithm 1 to all masks of the 1st compartment with $L = 3$. The resulting masks $m_{11}^{\perp}, m_{12}^{\perp},$ and $m_{13}^{\perp}$ are orthogonal to each other. The original mask m_{11} was greatly modified, whereas m_{12} and m_{13} were marginally modified.

66

Figure 4-5: A complete flow chart that demonstrates the metabolite map reconstruction process.

4.2 Methods

In this section, we assessed the performance of the proposed method using two data sets that include a numerical magnetic resonance spectroscopic imaging phantom and in vivo acquisitions. For each experiment, we used the proposed method to reconstruct the metabolite map from undersampled k-space mea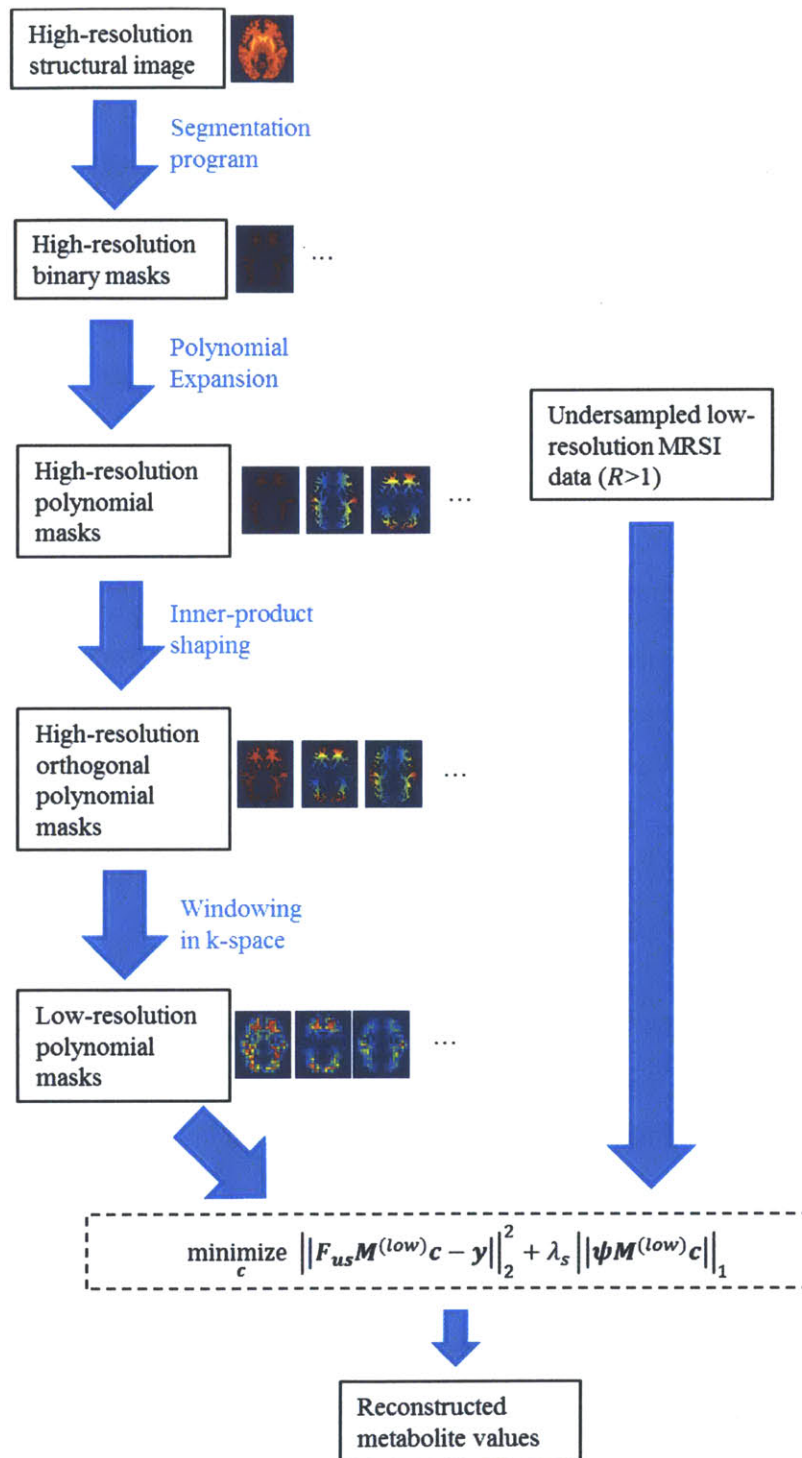surements with various acceleration factors R. Figure 4-6 shows an example of the undersampling pattern at an acceleration factor of 6.5 ($R = 6.5$) for a specific time point. The k-space data is sampled more densely in the middle due to its high energy at these locations. In this work, we used the same undersampling pattern for all time points in order to speed up the reconstruction process. Specifically, by using the same undersampling pattern, we reduce the dimension of the problem by one, which makes the reconstruction process considerably faster.

The results were quantitatively compared to those obtained from the least-squares method with the same undersampling pattern and acceleration factors. As opposed to the proposed algorithm, the least-squares method does not impose any prior information on the reconstruction process. We compared the performance of the proposed method to that of the conventional method by using the root-mean-square error (RMSE) of the reconstructed metabolite map as a criterion.

4.2.1 Numerical Magnetic Resonance Spectroscopic Imaging Phantom

In this experiment, the reconstructions were evaluated on the numerical magnetic resonance spectroscopic imaging phantom. We generated the numerical MRSI phantom in two steps: defining the tissue boundaries and generating the spectra. First, we defined the tissue boundaries of the phantom using the segmented structural image obtained from a healthy subject. Second, we generated the spectrum at each voxel using SPINEVOLUTION [40]. We assigned realistic values that were reported in [41, 42] to each peak in the spectrum (e.g., water, NAA, Cr, and Cho peaks) to make it become more realistic. The water component was generated with its peak being approximately ten times higher in amplitude than that of the NAA peak. There is no lipid in any spectrum.

We modeled the brain as a summation of nine compartments ($N = 9$). The boundaries of all compartments were obtained from the structural images using

Freesurfer [43]. The 0th order polynomial was used to create the mask for each compartment ($L = 1$). The Daubechies Wavelet of length 2 was used as a sparsifying transform. Noise-free metabolite maps were used as the ground truth. We chose the noise-free metabolite maps as opposed to the fully-sampled noisy metabolite maps in order to take into consideration the over-fitting problem. In other words, the reconstruction that does not fit the noise component is preferable.

The reconstructions were evaluated at acceleration factors of 3, 6, 9, and 12. For each acceleration factor, the Monte Carlo simulation was performed to propagate uncertainties in model inputs. Specifically, we reconstructed the metabolite maps and computed their corresponding RMSEs from 250 Monte Carlo trials with different realizations of the complex white Gaussian noise with the same standard deviation. The signal-to-noise ratio with respect to the averaged NAA peak from the spectra resided in the white matter is equal to ten.

4.2.2 In Vivo Data

Three data sets were obtained separately from a healthy human subject. They consist of water reference data, magnetic resonance spectroscopic imaging data, and T1-weighted structural images. The water reference and MRSI data were fully sampled at three Tesla using the LASER sequence [44]. The echo time (TE) and repetition time (TR) were 30 and 1800 milliseconds, respectively. The total scan times were one minute and eight minutes for the 1-average water reference and 4-averages MRSI data set, respectively. The field-of-view (FOV) of 24cm×24cm×8cm at 1 cm^3 isotropic was excited. The T1-weighted structural volume at 1 mm^3 isotropic resolution was also acquired in the same orientation in order to obtain the tissue boundaries that were later used as the prior information in the reconstruction process.

We used three compartments to model the brain ($N = 3$). The tissue boundaries were obtained from the T1-weighted structural images using FSL [45]. The first order polynomial was used to create masks for each compartment ($L = 3$). The Daubechies Wavelet of length 2 was used as a sparsifying transform. The water map and the metabolite maps consisting of NAA, creatine, and choline were reconstructed at an

acceleration factor equals to six on the post gridded-data. The reconstructed metabolite map from the fully-sampled least-squares reconstruction ($R = 1$) was used as the ground truth.
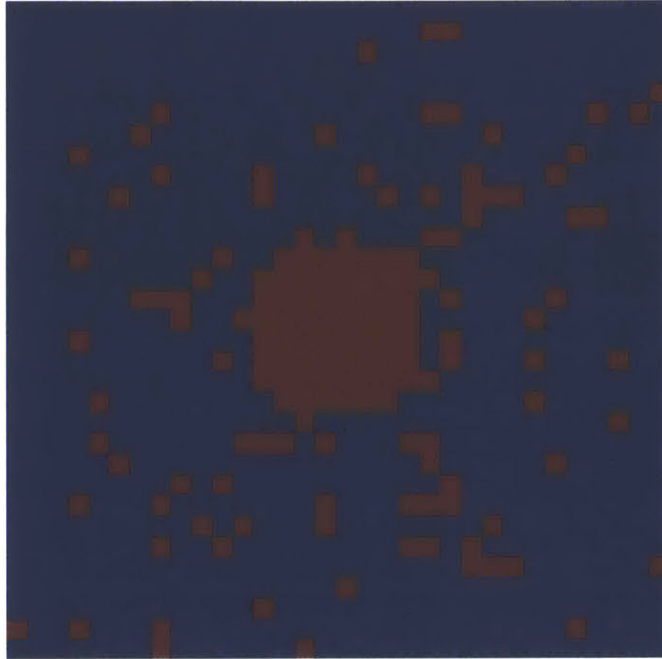
Undersampling pattern ($R = 6.5$)

Figure 4-6: An undersampling pattern at an acceleration factor of 6.5 ($R = 6.5$) for a specific time point. The k-space locations obtained are indicated in red. The k-space data is sampled more densely in the middle due to its high energy at these locations.

4.3 Results and Discussions

4.3.1 Numerical Magnetic Resonance Spectroscopic Imaging Phantom

Figure 4-7 presents %RMSE comparisons of the reconstructed NAA map from the least-squares (LS) algorithm and proposed algorithm at various acceleration factors. The proposed method yielded 3.85%, 5.16%, 5.52%, and 6.07% mean RMSEs, whereas the LS method yielded 4.83%, 7.84%, 10.29%, and 15.48% mean RMSEs at R = 3, 6, 9, and 12, respectively. The proposed method yielded the standard deviations of RMSE that were equaled to 0.65, 0.96, 1.03, and 1.02, whereas the LS method yielded the standard deviation of RMSE that were equaled 1.10, 1.74, 2.78, and 4.23 at R = 3, 6, 9, and 12, respectively.

The mean and the standard deviation of %RMSEs of the proposed method are smaller than those obtained from the LS method at all acceleration factors. Since we picked $L = 1$, both methods assumed that the metabolite values are constant within the same compartment. This assumption matched well with the characteristic of our specially designed numerical MRSI phantom. As seen in the same figure, the proposed method had much lower %RMSEs especially at high acceleration factors because it also imposed an additional prior on the data structure in the transform domain. In particular, it imposed the sparsity of the metabolite maps in the Wavelet domain. This choice of prior is appropriate because the metabolite map has only a few dominating coefficients in that domain, as shown in Figure 4-8. This additional prior knowledge prevented the algorithm from moving away from the true solution by narrowing down the search space. As a result, the proposed method not only converges faster, but also becomes more accurate and robust.

4.3.2 In Vivo Data

Figure 4-9 and Figure 4-10 present the maps in the same arrangement. They show the fully-sampled map from the data acquired from the scanner without any processing, reconstructed map from the least-squares (LS) method with $R = 1$, reconstructed map from the proposed method with $R = 6$, and reconstructed map from the LS method with R = 6, from left to right. Figure 4-9 shows the RMSE with respect to the fully-sampled LS

reconstruction (second map from the left) in the upper right hand corner of each reconstructed water map. The proposed method yielded 2.71% RMSE, whereas the LS method yielded 6.47% at $R = 6$. Figure 4-10 shows the RMSE with respect to the fully-sampled LS reconstruction (second map from the left) below each reconstructed metabolite map. For the NAA case, the proposed method yielded 8.31% RMSE, whereas the LS method yielded 10.10% at $R = 6$. For the creatine case, the proposed method yielded 6.33% RMSE, while the LS method yielded 12.13%. For the choline case, the proposed method yielded 9.34% RMSE, whereas the LS method yielded 13.91%. For any reconstruction method, the RMSE computed from the reconstructed water map was about two to three times lower than those from the reconstructed metabolite maps because the water signal has a relatively higher SNR compared to those of the metabolite signals.

On the one hand, we chose the 0th order polynomial masks in the numerical MRSI phantom case. On the other hand, we used the 1st order polynomial to generate the masks in the *in vivo* case because we observed that the metabolite values slowly vary within the same tissue type. Although the same polynomial was used in both the proposed and conventional LS methods, the proposed method yielded lower RMSEs in all cases compared to those using the LS method because the proposed method imposed an additional prior on the sparsity of the maps in the Wavelet domain. With this additional prior, the number of candidate solutions was significantly reduced leading to a faster convergence and more accurate reconstruction.
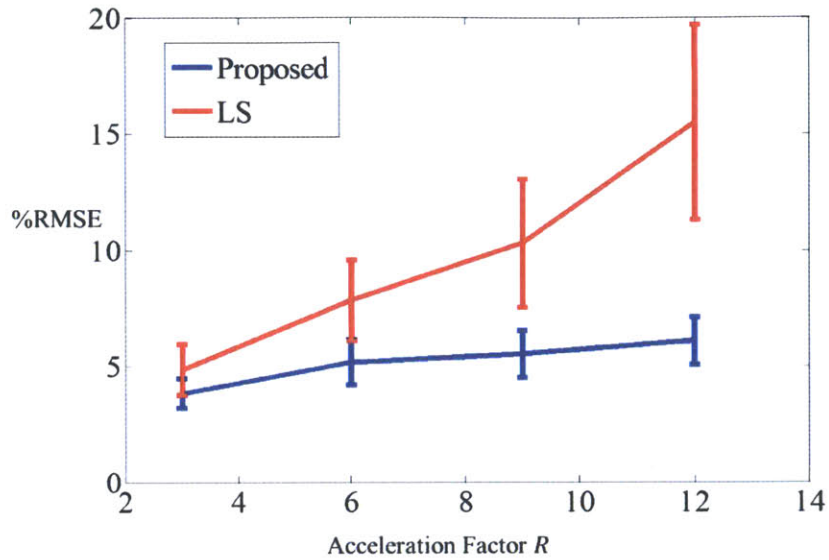
Figure 4-7: %RMSE comparison of the reconstructed NAA map from the least-squares (LS) algorithm and proposed algorithm at various acceleration factors (Numerical MRSI phantom with SNR = 10). The mean and standard deviation of %RMSEs shown in this figure were computed based on 250 Monte Carlo trials with different realization of the complex white Gaussian noise with the same variance.

NAA map in image domain

NAA map in Wavelet domain
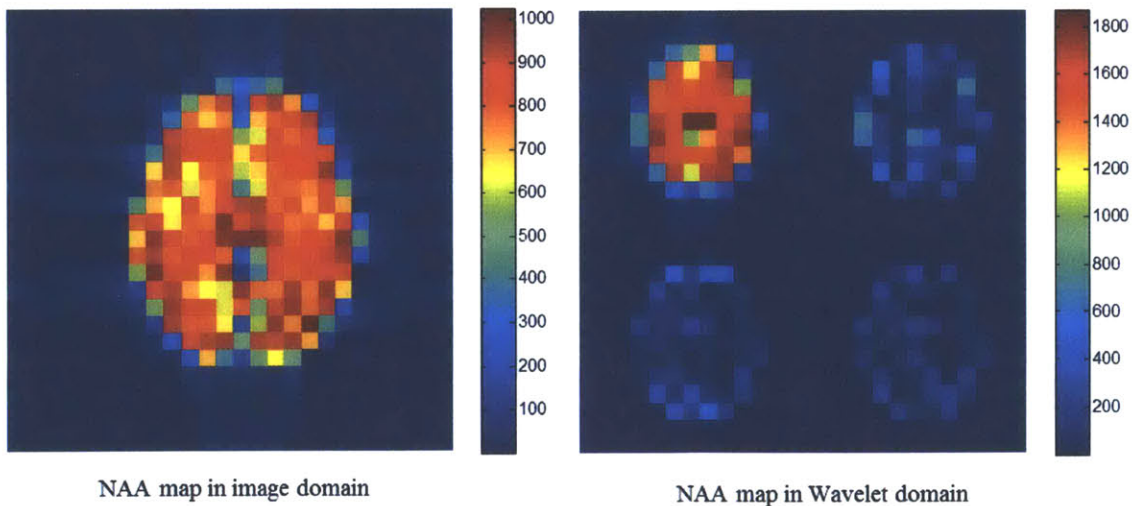
Figure 4-8: The low-resolution NAA map has only a few dominating coefficients in the Wavelet domain.

74
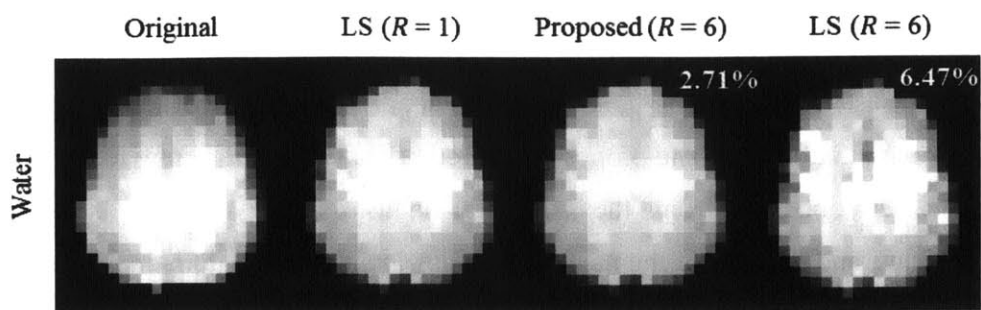
Figure 4-9: Water maps with corresponding RMSE. The fully-sampled map without any processing, the reconstructed map from the LS method with $R = 1$, reconstructed map from the proposed method with $R = 6$, and reconstructed map from the LS method with $R = 6$, from left to right.
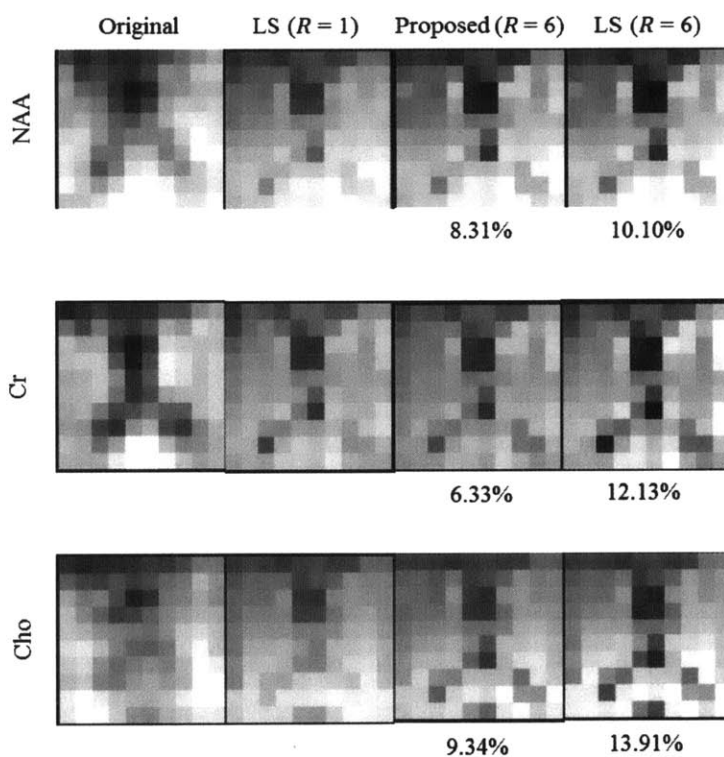
Figure 4-10: NAA (top row), creatine (middle row), and choline (bottom row) maps with corresponding RMSE. The fully-sampled map without any processing, the reconstructed map from the LS method ($R = 1$), proposed method ($R = 6$), and LS method ($R = 6$) from left to right.

4.4 Conclusion

This chapter presents the theory of the N-compartment-model method with the orthogonal polynomial masks. The proposed method exploits the prior knowledge of the tissue boundaries obtained from the structural images, slowly-varying nature of metabolite values, and sparsity of the metabolite maps in a transform domain. With these priors, the proposed method allows undersampling of k-space measurements, which results in a reduction in the scan time for the magnetic resonance spectroscopic imaging study, while it retains the high reconstruction quality. The experimental results show that the proposed method is superior to the conventional method because of its robustness and higher reconstruction accuracy.

Bibliography

1.   Gagoski, B.A., *Magnetic resonance spectroscopic imaging using parallel transmission at 7T.* PhD Thesis, Massachusetts Institute of Technology, 2011.

2.   Spielman, D.M., *Magnetic Resonance Metabolic Imaging.* PhD Thesis, Stanford University, 1990.

3.   Ratai, E., et al., *Seven-Tesla proton magnetic resonance spectroscopic imaging in adult X-linked adrenoleukodystrophy.* Arch Neurol, 2008. **65**(11): p. 1488-94.

4.   Adalsteinsson, E., et al., *Gray matter N-acetyl aspartate deficits in secondary progressive but not relapsing-remitting multiple sclerosis.* AJNR Am J Neuroradiol, 2003. **24**(10): p. 1941-5.

5.   Cifelli, A., et al., *Thalamic neurodegeneration in multiple sclerosis.* Ann Neurol, 2002. **52**(5): p. 650-3.

6.   Pfefferbaum, A., et al., *In vivo brain concentrations of N-acetyl compounds, creatine, and choline in Alzheimer disease.* Arch Gen Psychiatry, 1999. **56**(2): p. 185-92.

7.   Schuff, N., et al., *Changes of hippocampal N-acetyl aspartate and volume in Alzheimer's disease. A proton MR spectroscopic imaging and MRI study.* Neurology, 1997. **49**(6): p. 1513-21.

8.   Stockler, S., et al., *Creatine deficiency in the brain: a new, treatable inborn error of metabolism.* Pediatr Res, 1994. **36**(3): p. 409-13.

9.   Sijens, P.E., et al., *1H MR spectroscopy in patients with metastatic brain tumors: a multicenter study.* Magn Reson Med, 1995. **33**(6): p. 818-26.

10.   Nelson, S.J., *Multivoxel magnetic resonance spectroscopy of brain tumors.* Mol Cancer Ther, 2003. **2**(5): p. 497-507.

11.   Higuchi, T., et al., *Mapping of lactate and N-acetyl-L-aspartate predicts infarction during acute focal ischemia: in vivo 1H magnetic resonance spectroscopy in rats.* Neurosurgery, 1996. **38**(1): p. 121-9; discussion 129-30.

12.   Nishimura, D.G., *Principles of Magnetic Resonance Imaging.* 1996.

13.   Kok, T., *Detection of Brain Metabolites in Magnetic Resonance Spectroscopy.* MS Thesis, Massachusetts Institute of Technology, 2008.

14. Posse, S., et al., *MR spectroscopic imaging: Principles and recent advances.* J Magn Reson Imaging, 2012.

15. Bilgic, B., et al., *Lipid suppression in CSI with spatial priors and highly undersampled peripheral k-space.* Magn Reson Med, 2012.

16. Ebel, A., V. Govindaraju, and A.A. Maudsley, *Comparison of inversion recovery preparation schemes for lipid suppression in 1H MRSI of human brain.* Magn Reson Med, 2003. **49**(5): p. 903-8.

17. Spielman, D.M., et al., *Lipid-suppressed single- and multisection proton spectroscopic imaging of the human brain.* J Magn Reson Imaging, 1992. **2**(3): p. 253-62.

18. Le Roux, P., et al., *Optimized outer volume suppression for single-shot fast spin-echo cardiac imaging.* J Magn Reson Imaging, 1998. **8**(5): p. 1022-32.

19. Luo, Y., et al., *BISTRO: an outer-volume suppression method that tolerates RF field inhomogeneity.* Magn Reson Med, 2001. **45**(6): p. 1095-102.

20. Bottomley, P.A., *Spatial Localization in Nmr-Spectroscopy Invivo.* Annals of the New York Academy of Sciences, 1987. **508**: p. 333-348.

21. Spielman, D., et al., *H-1 Spectroscopic Imaging Using a Spectral Spatial Excitation Pulse.* Magnetic Resonance in Medicine, 1991. **18**(2): p. 269-279.

22. Hetherington, H.P., et al., *Quantitative 1H spectroscopic imaging of human brain at 4.1 T using image segmentation.* Magn Reson Med, 1996. **36**(1): p. 21-9.

23. Lim, K.O. and D.M. Spielman, *Estimating NAA in cortical gray matter with applications for measuring changes due to aging.* Magn Reson Med, 1997. **37**(3): p. 372-7.

24. Pfefferbaum, A., et al., *In vivo spectroscopic quantification of the N-acetyl moiety, creatine, and choline from large volumes of brain gray and white matter: effects of normal aging.* Magn Reson Med, 1999. **41**(2): p. 276-84.

25. Lustig, M., D. Donoho, and J.M. Pauly, *Sparse MRI: The application of compressed sensing for rapid MR imaging.* Magn Reson Med, 2007. **58**(6): p. 1182-95.

26. Adalsteinsson, E., et al., *Volumetric spectroscopic imaging with spiral-based k-space trajectories.* Magn Reson Med, 1998. **39**(6): p. 889-98.

27.   Oppenheim, A.V. and R.W. Schafer, *Discrete-time signal processing*. 3rd ed. Prentice Hall signal processing series2010, Upper Saddle River N.J.: Pearson. xxviii, 1108 p.

28.   Axler, S.J., *Linear algebra done right*. 2nd ed. Undergraduate texts in mathematics1997, New York: Springer. xv, 251 p.

29.   Boyd, S.P. and L. Vandenberghe, *Convex optimization*2004, Cambridge, UK ; New York: Cambridge University Press. xiii, 716 p.

30.   Candès, E.J. *Compressive Sampling*. in *International Congress of Mathematicians*. 2006. Madrid, Spain.

31.   Weller, D.S., *Accelerating Magnetic Resonance Imaging by Unifying Sparse Models and Multiple Receivers*, 2012, Massachusetts Institute of Technology.

32.   Bao, Y. and A.A. Maudsley, *Improved reconstruction for MR spectroscopic imaging*. IEEE Trans Med Imaging, 2007. **26**(5): p. 686-95.

33.   Eslami, R. and M. Jacob, *Robust reconstruction of MRSI data using a sparse spectral model and high resolution MRI priors*. IEEE Trans Med Imaging, 2010. **29**(6): p. 1297-309.

34.   Hu, X., et al., *SLIM: spectral localization by imaging*. Magn Reson Med, 1988. **8**(3): p. 314-22.

35.   Jacob, M., et al., *Improved model-based magnetic resonance spectroscopic imaging*. IEEE Trans Med Imaging, 2007. **26**(10): p. 1305-18.

36.   Khalidov, I., et al., *BSLIM: spectral localization by imaging with explicit B0 field inhomogeneity compensation*. IEEE Trans Med Imaging, 2007. **26**(7): p. 990-1000.

37.   Liang, Z.P. and P.C. Lauterbur, *A generalized series approach to MR spectroscopic imaging*. IEEE Trans Med Imaging, 1991. **10**(2): p. 132-7.

38.   Strang, G., *Linear algebra and its applications*. 4th ed2006, Belmont, CA: Thomson, Brooks/Cole. viii, 487 p.

39.   Eldar, Y.C., *Least-squares inner product shaping*. Linear Algebra and Its Applications, 2002. **348**: p. 153-174.

40.   Veshtort, M. and R.G. Griffin, *SPINEVOLUTION: a powerful tool for the simulation of solid and liquid state NMR experiments*. J Magn Reson, 2006. **178**(2): p. 248-82.

41.   Frahm, J., et al., *Localized proton NMR spectroscopy in different regions of the human brain in vivo. Relaxation times and concentrations of cerebral metabolites.* Magn Reson Med, 1989. **11**(1): p. 47-63.

42.   Minati, L., et al., *Quantitation of normal metabolite concentrations in six brain regions by in-vivoH-MR spectroscopy.* J Med Phys, 2010. **35**(3): p. 154-63.

43.   Fischl, B., et al., *Whole brain segmentation: automated labeling of neuroanatomical structures in the human brain.* Neuron, 2002. **33**(3): p. 341-55.

44.   Garwood, M. and L. DelaBarre, *The return of the frequency sweep: designing adiabatic pulses for contemporary NMR.* J Magn Reson, 2001. **153**(2): p. 155-77.

45.   Zhang, Y., M. Brady, and S. Smith, *Segmentation of brain MR images through a hidden Markov random field model and the expectation-maximization algorithm.* IEEE Trans Med Imaging, 2001. **20**(1): p. 45-57.